SLAC–PUB–7844
June 1998

Measurement and Correction of Accelerator Optics*

F. Zimmermann

Stanford Linear Accelerator Center
Stanford University, Stanford, CA 94309, USA

This report reviews procedures and techniques for measuring, correcting and controlling various optics parameters of an accelerator, including the betatron tune, beta function, betatron coupling, dispersion, chromaticity, momentum compaction factor, and beam orbit. The techniques described are not only indispensable for the basic set-up of an accelerator, but in addition the same methods can be used to study more esoteric questions as, for instance, dynamic aperture limitations or wakefield effects. The different procedures are illustrated by examples from several accelerators, storage rings as well as linacs and transport lines.

Presented at the
Joint US-CERN-Japan-Russian School on Beam Measurement,
Montreux, Switzerland, May 11–20, 1998

*Work supported by the U.S. Department of Energy contract DE–AC03–76SF00515.

MEASUREMENT AND CORRECTION OF ACCELERATOR OPTICS [a]

F. ZIMMERMANN
Stanford Linear Accelerator Center,
Stanford University, Stanford, California 94309

We review procedures and techniques for measuring, correcting and controlling various optics parameters of an accelerator, including the betatron tune, beta function, betatron coupling, dispersion, chromaticity, momentum compaction factor, and beam orbit. The techniques described are not only indispensable for the basic set-up of an accelerator, but in addition the same methods can be used to study more esoteric questions as, for instance, dynamic aperture limitations or wakefield effects. The different procedures are illustrated by examples from several accelerators, storage rings as well as linacs and transport lines.

Contents

[a] Work supported by the U.S. Department of Energy under contract DE-AC03-76SF00515.

1 Introduction

This report describes techniques for measuring, correcting and controlling the optics of an accelerator, such as methods to measure betatron tunes, betatron phase advance, beta function, transverse coupling, dispersion, momentum compaction factor, and chromaticity. It also discusses matching of beta functions and dispersion in a transport line, identification of quadrupole errors, beam-based alignment and orbit correction. In addition, a few important mathematical algorithms are presented, such as fitting techniques based on eigenvalue analysis and singular value decomposition.

The different techniques are illustrated by examples from various accelerators: the large electron-positron collider LEP at CERN [1], the SLAC PEP-II B factory [2], the linac of the KEK B factory [3], the Stanford Linear Collider (SLC) [4,5], TRISTAN at KEK [6], the synchrotron light source SPEAR at SLAC [7], the Accelerator Test Facility (ATF) at KEK [8], the electron-positron collider

HERA at DESY [9], the final-focus test beam at SLAC [10], the CERN $p\bar{p}$ collider SPS [11], the ASSET experiment at SLAC [12], and the ISR at CERN [13].

2 Review of Transverse Linear Optics

In linear approximation, the transverse motion of a single particle in an accelerator can be described as the sum of three components [14,15]

$$u(s) = u_{c.o.}(s) + u_\beta(s) + \eta(s)\delta \tag{1}$$

where $u_\beta(s) = x$ or y is the horizontal or vertical coordinate at the (azimuthal) location s, and $u_{c.o.}$ denotes the closed equilibrium orbit (or, in a transport line, some reference trajectory), u_β the orbit variation due to betatron motion (transverse oscillations), and $\eta\delta$ the orbit change resulting from an energy offset; η is the dispersion function, and $\delta = \Delta p/p$ the relative deviation from the design momentum.

The betatron motion can be parametrized by a pseudo-harmonic oscillation of the form [14]

$$u_\beta(s) = \sqrt{2I_{x,y}\beta_{x,y}(s)}\ \cos(\phi_{x,y}(s) + \phi_0) \tag{2}$$

where $\beta_{x,y}(s)$ is called the beta function, $\phi_{x,y}(s)$ the betatron phase, and $I_{x,y}$ is an action variable. The functions $\phi_{x,y}(s)$ and $\beta_{x,y}(s)$ depend on the azimuthal location s, while the action $I_{x,y}$ and initial phase ϕ_0 are constants of motion. The value of $I_{x,y}$ averaged over all particles of a beam is equal to the rms beam emittance, $\epsilon_{x,y}^{rms} =< I_{x,y} >$. The 'betatron oscillation' described by Eq. (2) refers to a particle at a fixed design energy. Later, in Sections 8 and 10 we will discuss how the motion is modified if the energy is not constant, presenting the two concepts of dispersion and chromaticity. Furthermore, when the beam is accelerated, as in a linac, Eq. (2) must be multiplied by a factor $\sqrt{\gamma(0)/\gamma(s)}$, since the increase in longitudinal momentum p_s reduces the transverse beam size (it effectively introduces a damping force $d^2u/ds^2 \approx -p_u/p_s^2\ dp_s/ds$).

In addition to the beta function β, two closely related functions are often introduced to characterize the betatron motion. These are

$$\alpha(s) = -\frac{1}{2}\beta'(s) \qquad \text{and} \qquad \gamma(s) = \frac{1+\alpha^2(s)}{\beta(s)} \tag{3}$$

where the prime indicates a derivative with respect to the longitudinal position s, and we have dropped the subindex 'x, y'. Henceforth, we will use x instead of u, but, here and in the following, the same equations apply in the horizontal and in the vertical plane. The main difference is that quadrupoles which are focusing in one plane are defocusing in the other. Finally note that if

the location is inside a linac accelerating structure the formula for α reads $\alpha(s) = (-\beta'(s)/2 + \beta E'(s)/(2E(s)))$, where $E(s)$ is the beam energy at location s.

The three optical functions $\beta(s)$, $\alpha(s)$ and $\gamma(s)$ are proportional to the three second moments of the beam distribution, with the beam emittance as constant of proportionality:

$$< x^2 >_s = \beta(s)\ \epsilon \tag{4}$$

$$< xx' >_s = -\alpha(s)\ \epsilon \tag{5}$$

$$< x'^2 >_s = \gamma(s)\ \epsilon \tag{6}$$

where $< \ldots >_s$ denotes an average over the beam distribution at the location s. Thus, the actual values of β, α and γ can be deduced from the measured beam distribution. It is a challenge to the accelerator physicist to make them coincide with their design values.

In a storage ring, the optical functions α, β and γ are periodic: $\beta(s) = \beta(s+L)$, $\alpha(s) = \alpha(s+L)$, and $\gamma(s) = \gamma(s+L)$, where L is the ring circumference. For a transport line, or linac, no such periodic boundary condition exists; so the values of the optical functions depend on the incoming beam distribution.

An alternative description represents the motion of a single particle in terms of a transport matrix [16,17]. Here, a trajectory is given by a point in phase space (x, x') which is transformed from the initial location i to a new (final) location f through a linear transformation

$$\begin{pmatrix} x \\ x' \end{pmatrix}_f = \begin{pmatrix} R_{11} & R_{12} \\ R_{21} & R_{22} \end{pmatrix}_{fi} \begin{pmatrix} x \\ x' \end{pmatrix}_i . \tag{7}$$

This can also be generalized to a 6×6 transport matrix for motion with coupling between the horizontal, vertical and longitudinal planes. In the 6-dimensional case, the vector (x, x') is replaced by $(x, x', y, y', z, \delta)$, where δ, the relative energy error, and z, the longitudinal distance to a reference particle, are the coordinates in the longitudinal phase space.

Let us look at a few examples. For a drift space of length L, the 2-dimensional transport matrix is

$$\mathbf{R}_{drift} = \begin{pmatrix} 1 & L \\ 0 & 1 \end{pmatrix}. \tag{8}$$

The matrix for a focusing quadrupole of gradient $K = (\partial B/\partial x)/(B\rho)$ and of length l_q is

$$\mathbf{R}_{quad} = \begin{pmatrix} \cos\phi & \sin\phi/\sqrt{|K|} \\ -\sqrt{|K|}\sin\phi & \cos\phi \end{pmatrix} \tag{9}$$

where $\phi = l_q\sqrt{|K|}$. If we take the limit of vanishing quadrupole length $l_{quad} \to 0$, while holding the integrated gradient $k = |K|l_q$ constant, we arrive at the matrix for an idealized 'thin-lens' quadrupole

$$\mathbf{R}_{thin-lens} = \begin{pmatrix} 1 & 0 \\ -k & 1 \end{pmatrix}. \tag{10}$$

Thus, the focal length of the thin quadrupole is given by $1/k$. The R matrix for a sequence of quadrupoles and drift spaces is simply the product of the R matrices for the individual elements.

It is important to note that the description in terms of optical functions and the R matrix formalism are equivalent and complementary: we can transform the optical functions from one location to another using the elements of the R matrix:

$$\begin{pmatrix} \beta \\ \alpha \\ \gamma \end{pmatrix}_f = \begin{pmatrix} R_{11}^2 & -2R_{11}R_{12} & R_{12}^2 \\ -R_{11}R_{21} & 1+2R_{12}R_{21} & -R_{12}R_{22} \\ R_{21}^2 & -2R_{21}R_{22} & R_{22}^2 \end{pmatrix}_{fi} \begin{pmatrix} \beta \\ \alpha \\ \gamma \end{pmatrix}_i \tag{11}$$

Alternatively, we can express the elements of the R matrix from i to f in terms of the optical functions at the initial and final locations,

$$\mathbf{R}_{fi} = \begin{pmatrix} \sqrt{\frac{\beta_f}{\beta_i}}(\cos\phi_{fi} + \alpha_i \ \sin\phi_{fi}) & \sqrt{\beta_f\beta_i}\ \sin\phi_{fi} \\ -\frac{1+\alpha_f\alpha_i}{\sqrt{\beta_f\beta_i}}\ \sin\phi_{fi} + \frac{\alpha_i-\alpha_f}{\sqrt{\beta_f\beta_i}}\ \cos\phi_{fi} & \sqrt{\frac{\beta_i}{\beta_f}}\ (\cos\phi_{fi} - \alpha_f\ \sin\phi_{fi}) \end{pmatrix}, \tag{12}$$

where $\phi_{fi} = (\phi_f - \phi_i)$ is the betatron phase advance between the two locations.

3 Betatron Tune

3.1 Introduction

In a storage ring, the Q value, or betatron tune, is defined as the number of betatron oscillations per revolution (often it is also called ν):

$$Q = \frac{\phi(L)}{2\pi} = \frac{1}{2\pi} \oint_L \frac{ds}{\beta(s)} \tag{13}$$

where the integral is taken around the ring of circumference L. The integer part of the tune Q is easily inferred from the orbit distortion induced by exciting a single steering corrector. This orbit distortion is essentially a betatron oscillation; thus, counting the number of oscillation periods around the

ring determines the integer value of the tune. A more intricate method, discussed in Section 4, is to perform a harmonic analysis of betatron oscillations recorded by multi-turn beam-position monitors. Thereby the betatron phase advance between adjacent BPMs can be determined, and the total phase advance around the ring gives the tune. If the integer part of the tune agrees with model predictions, large optics errors can be ruled out. More important than the integer value of the tune is its fractional part, since the latter can have a strong effect on beam lifetime or emittance.

Tune measurements are useful for quite a variety of applications: the tune shift with quadrupole strength gives the local beta function, the tune shift with rf frequency the chromaticity, the tune shift with current the effective transverse impedance, and the tune shift with betatron amplitude the strength of the nonlinear fields. Further, optimizing and controlling the tunes improves the beam lifetime and the dynamic aperture, and it can reduce beam loss or emittance growth during acceleration. For example, Fig. 1 shows the variation of the extracted vertical beam size as a function of the vertical betatron tune which was measured at the SLC electron damping ring.

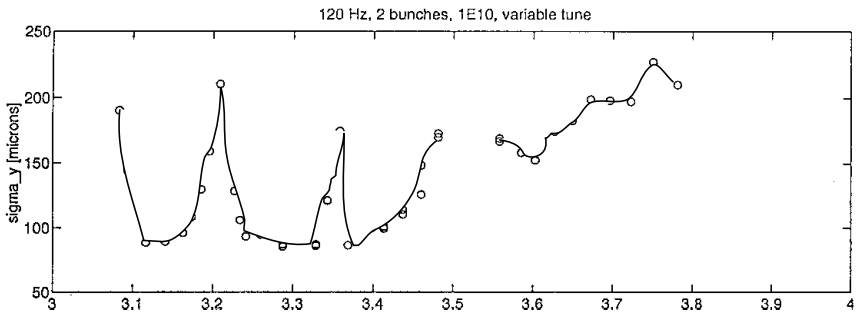

Figure 1: Rms vertical size of the electron beam extracted from the SLC damping ring as a function of the vertical betatron tune. This measurement was performed under unusually poor vacuum conditions [18]. (Courtesy M. Minty, 1998.)

Also space charge, ionized gas molecules, beam-beam interaction and radiation damping can affect the tune signal, for example, the shape of the beam response to a swept-frequency excitation. An example for the dramatic effect of the nonlinear beam-beam force is shown in Fig. 2. In addition, fast decoherence and filamentation, head-tail damping or instabilities may make it difficult to extract a clean and reproducible tune signal. On the other hand, this also implies that all these processes can be studied by means of tune measurements.

In the following we will describe three approaches to measure the frac-

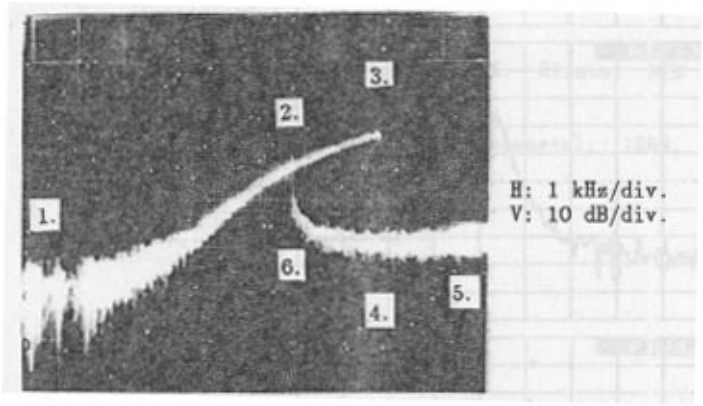

Figure 2: Transverse tune measurement (swept-frequency excitation) with 2 colliding bunches at Tristan [19]. (Courtesy K. Hirata, 1998.)

tional part of the tune. These approaches fall into two different categories: (1) precision tune measurements and (2) tune tracking (to monitor and control fast changes, *e.g.*, during acceleration). For simplicity, the fractional part of the tune will also be denoted by Q.

3.2 Fast Fourier Transform (FFT)

A common method to measure the fractional part of the betatron tune is to excite transverse beam motion and to detect the transverse beam position over a number of successive turns N. The excitation may consist of white noise or a single kick. Beam oscillations caused by injection are also often used, in order not to interfere with the machine operation. The power density of the detected signal is computed via a Fourier transformation, and the betatron tunes are identified as the frequencies with the highest amplitude peak (this is not always the case, as sometimes the beam is strongly excited at other frequencies). Figure 3 shows typical multi-turn BPM measurements. Alternatively, a spectrum analyzer could be used to frequency analyze the detected signal.

A Fourier analysis uses a time series $x(1),\ x(2), ..., x(N)$ of N orbit measurements for consecutive turns as input. This time series is expanded as a linear combination of N orthonormal functions,

$$x(n) = \sum_{j=1}^{N} \psi(Q_j)\ \exp(2\pi i n Q_j). \tag{14}$$

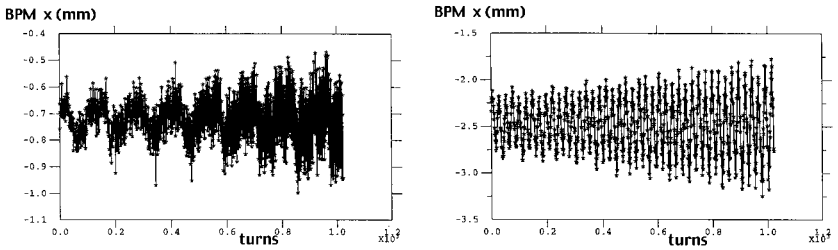

Figure 3: Multi-turn orbit measurement for the motion of the 500th bunch in a train of 1760 bunches at PEP-II. Shown are horizontal BPM orbit readings as a function of turn number: (Left) BPM in a dispersive region; (right) BPM in a non-dispersive region. For this number of bunches at high current the beam was self-excited. The slow oscillation in the upper picture corresponds to energy (or synchrotron) oscillations. The fast oscillations are the betatron motion. The corresponding FFT spectra are displayed in Fig. 4. (Courtesy U. Wienands, J. Seeman *et al*, 1998.)

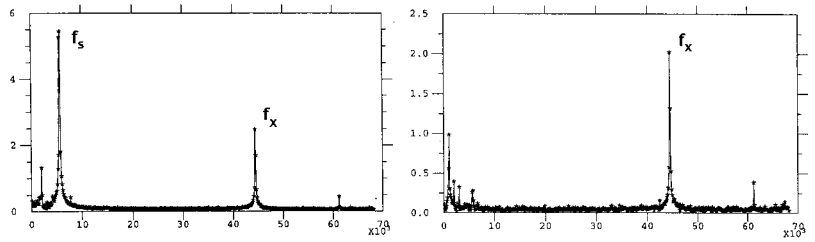

Figure 4: FFT spectra for the two BPM measurements of Fig. 3 in a dispersive (left) and in a nondispersive region (right). (Courtesy U. Wienands, J. Seeman *et al*, 1998.)

The expansion can be done efficiently with a Fast Fourier Transform algorithm. The frequency corresponding to the largest value of ψ is taken as the approximate tune (see Fig. 4). The error due to the discreteness of the frequency steps is equal to

$$|\delta Q| \leq \frac{1}{2N} \tag{15}$$

Thus, to obtain a tune value with a resolution of 0.001 or better using Eq. (14) requires orbit data for about 1000 turns. As an illustration, Fig. 4 displays FFT spectra of the orbit motion measured at the two BPMs of Fig. 3. The FFT demonstrates that a large part of the orbit motion in the dispersive region is due to synchrotron oscillations.

Interpolated FFT

If we use a simple Fourier analysis based on the peak amplitude of ψ in Eq. (14), typically we need about 1000 turns of orbit data to obtain an adequate tune resolution. During this time the beam could filament or the oscillation amplitude could decrease significantly, giving rise to spurious results. Fortunately, interpolating the shape of the Fourier spectrum around the main peak improves the resolution quite dramatically[20]. Thereby the same resolution can be achieved by processing data for a much smaller number of turns.

The basic idea is that the shape of the Fourier spectrum is known, and equal to that of a pure sinusoidal oscillation with tune Q_{Fint},

$$|\psi(Q_j)| = \left| \frac{\sin N\pi(Q_{Fint} - Q_j)}{N \sin \pi(Q_{fint} - Q_j)} \right| \tag{16}$$

The formula for the interpolated tune Q_{Fint} reads[21]:

$$Q_{Fint} = \frac{k}{N} + \frac{1}{\pi} \arctan \left(\frac{|\psi(Q_{k+1})| \sin\left(\frac{\pi}{N}\right)}{|\psi(Q_k| + |\psi(Q_{k+1})| \cos\left(\frac{\pi}{N}\right)} \right) \tag{17}$$

where $|\psi(Q_k)|$ is the peak of the Fourier spectrum in Eq. (14), and $|\psi(Q_{k+1})|$ its highest neighbor. So, instead of using only the peak value of the FFT, one interpolates between the two highest points. For large N the error is given by

$$|\delta Q| \leq \frac{C_{Fint}}{N^2} \tag{18}$$

where C_{Fint} is a numerical constant. So, the resolution improves quadratically with the number of turns, and already from a beam signal recorded over 30–60 turns fairly accurate tune values can be obtained. For $N \gg 1$, Eq. (17) may be approximated by the simpler form[20]

$$Q_{Fint} \approx \frac{k}{N} + \frac{1}{N} \arctan \left(\frac{|\psi(Q_{k+1})|}{|\psi(Q_k| + |\psi(Q_{k+1})|} \right) \tag{19}$$

Interpolated FFT with Data Windowing

The accuracy of the Fourier analysis can be further improved with data windowing[22,21]. Here, the data $x(n)$ are weighted with filter functions $\chi(n)$ before the interpolated FFT is applied. The Fourier coefficients of the filtered signal are

$$\psi(Q_j) = \frac{1}{N} \sum_{i=1}^{N} x(n)\chi(n) \exp(-2\pi i n Q_j) \tag{20}$$

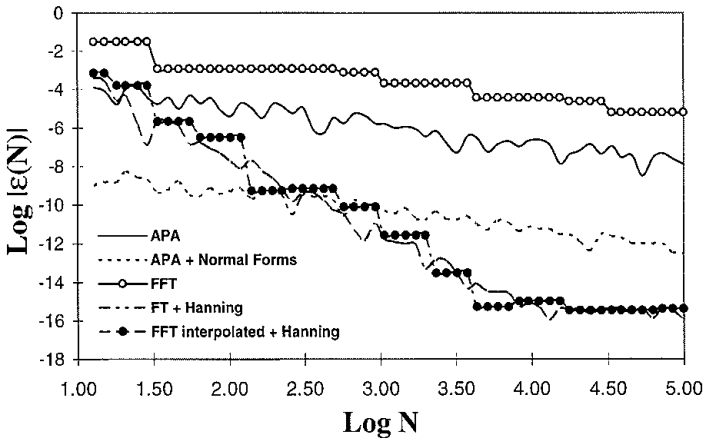

Figure 5: Tune precision vs. number of turns, considering different FFT techniques applied to tracking data for the 4-D Hénon map [21]. The abbreviation 'APA' refers to a calculation of the average phase advance, which can be computed either in the original phase-space coordinates or in so-called normal-form coordinates. See Ref. [21] for more details on these alternative methods. (Courtesy M. Giovannozzi, 1998.)

Applying a Hanning-like filter of order l, $\chi_l(n) = A_l \sin^l(\pi n/N)$ with A_l some normalization constant, in the limit $N \gg 1$ the interpolated tune reads

$$Q_{Fint} = \frac{k}{N} + \frac{1}{N}\left(\frac{(l+1)\psi(Q_{n+1})}{\psi(Q_n)+\psi(Q_{n+1})} - \frac{l}{2}\right) \tag{21}$$

The resolution improves with the $(l+2)$th power of the number of samples N:

$$|\delta Q| \leq \frac{C_{FHan}}{N^{l+2}} \tag{22}$$

where C_{FHan} again is a numerical constant.

An example comparing the precision of different FFT procedures is shown in Fig. 5 [21], which clearly demonstrates the superiority of the interpolated FFT with data windowing (Hanning filter). Unfortunately, the beneficial effect of the Hanning filter disappears when the signal contains a small noise component [21], in which case the resolution decreases as $\sim N^{-2}$ only, just as with the simple interpolated FFT.

3.3 Swept-Frequency Excitation

A different method to measure the tune is to excite the beam with a steady sinusoidal wave and to detect the amplitude and phase of the beam response. The excitation frequency is increased in steps. The strength of the harmonic excitation is adjusted so as to produce beam oscillations of adequate amplitude at the resonant frequency.

The result of this measurement is a 'transverse beam-transfer function', which is the (complex) response of the beam to a harmonic excitation as a function of frequency. The beam-transfer function contains important information, for example, about the transverse impedance or about radiation damping[23]. It is easy to see from Eq. (14) that, in frequency domain, the tune signal repeats itself in frequency intervals corresponding to multiples of the revolution frequency f_{rev} (*i.e.*, a spectrum analysis of the signal from one pick up contains no information about the integer part of the tune). If n_b equidistant bunches are stored in a ring and the combined signal of all bunches is detected, the periodicity of the FFT signal is $n_b f_{rev}$. In addition, the tune spectrum from 0 to $n_b f_{rev}/2$ and that from $n_b f_{rev}/2$ to $n_b f_{rev}$ are mirror images of each other. Therefore, for the study of multibunch instabilities, it is sufficient to measure the beam transfer function around each revolution harmonic between zero and $n_b f_{rev}/2$.

The concept of the beam-transfer function can be extended to higher-order beam excitations. At the CERN AA a quadrupole detector and a quadrupole pick-up were used to measure the quadrupole mode beam-transfer function of an antiproton beam[24].

The frequency-sweep method as discussed so far requires a relatively long time in order to measure the response at each frequency with sufficient accuracy. However, there exists a fast version of this method, called a chirp excitation. Here the frequency of the excitation is ramped rapidly across the tune resonance, while the beam response is observed[25]. This is useful to monitor fast tune changes, as, for instance, during acceleration in the SPS[26].

3.4 Phase Locked Loop

While exactly at the betatron tune the amplitude of the beam-transfer function has zero slope as a function of excitation frequency, the phase of the beam-response has maximum slope. The phase difference between excitation and beam motion changes from 0 degree to 180 degree when the excitation frequency is ramped through the resonance. Directly at the betatron tune, the phase difference is 90 degrees. The phase can be monitored continually by a phase locked loop circuit (PLL); see, *e.g.*, Ref.[25,27].

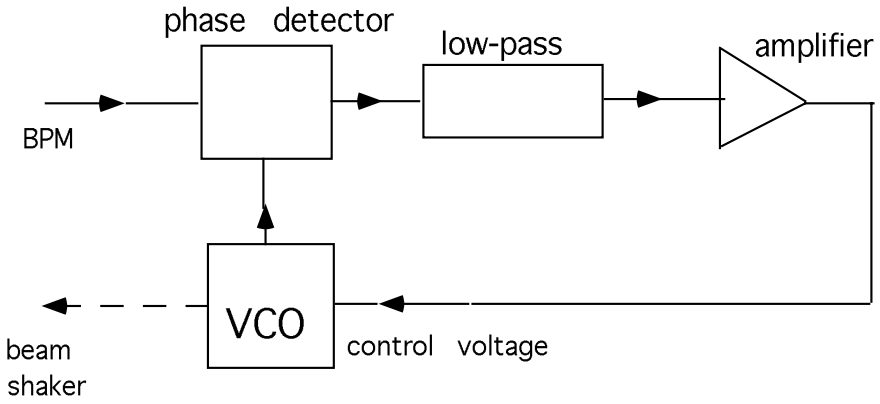

Figure 6: Schematic of phase locked loop for continuous tune control.

The signal flow diagram of a phase locked loop is sketched in Fig. 6. The phase detector compares the frequency of a beam position signal, *e.g.*, from a BPM, with the frequency of a local oscillator. The phase-detector output voltage is a measure of the frequency difference of its two input signals. After low-pass filtering and amplification, this signal is used to adjust the frequency of the local oscillator (VCO), such that the oscillator 'locks' to the frequency of the input beam signal. The oscillator frequency serves as the betatron tune signal which is displayed or processed by the accelerator control system. Sometimes the oscillator signal is also used to excite the beam, in which case the phase locked loop becomes part of a 'lock-in amplifier'. PLL circuits allow a continuous tracking of the time evolution of the betatron tune.

3.5 Schottky Monitor

All the techniques reported so far measured the coherent betatron tune, *i.e.*, the oscillation frequency of the beam centroid. In the case of proton beams it is also possible to measure the incoherent betatron tune, *i.e.*, the oscillation frequency of individual particles in the beam (in the absence of centroid motion). The incoherent signal is proportional to $\sqrt{\epsilon\ N\ \Delta f}$, where ϵ is the beam emittance, N the number of particles in the beam, and Δf a frequency bandwidth. Though this signal is small, it can be detected with sensitive 'Schottky monitors'[28].

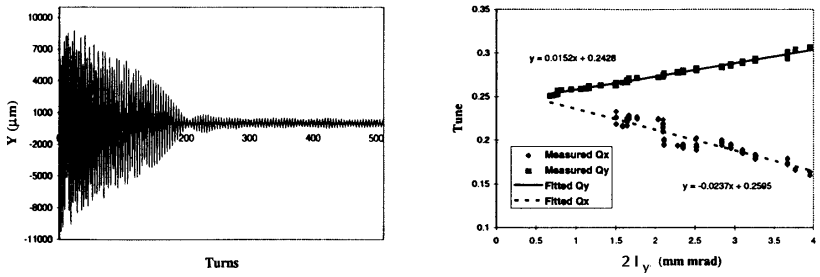

Figure 7: Measurement of tune shift with amplitude in LEP at 20 GeV, using a high-precision FFT tune analysis [29]: (left) vertical oscillation amplitude after a kick; (right) horizontal and vertical betatron tunes vs. twice the vertical action variable I_y of the beam centroid motion. The observed tune shift with amplitude was consistent with the expected effect of the sextupole and octupole field components in the dipole magnets. (Courtesy R. Bartolini, 1998.)

3.6 Application: Nonlinear Dynamics Studies

For studies of nonlinear dynamics a multi-turn BPM readout is a great advantage. Three examples may illustrate this point.

Tune Shift with Amplitude: The interpolated FFT with data windowing was applied at LEP and SPEAR to measure the tune shift with betatron amplitude [29]. The latter is of interest since it carries information about the nonlinear fields experienced by the beam, that may affect the beam stability and lifetime. Any nonlinear field can cause a tune shift with amplitude; these nonlinear fields change the average focusing experienced by a particle executing large betatron oscillations.

In the LEP experiment, the beam was kicked in the vertical plane, and the tune was calculated over successive short time windows, of 32 turns each, as the beam oscillation damped rapidly. Figure 7 shows a result for LEP at 20 GeV. In Fig. 7 (left), the vertical beam position is displayed as a function of time demonstrating the fast damping, over 200 turns. The shift of the horizontal and vertical betatron tune with the vertical action variable, as computed over 32-turns time windows is presented in Fig. 7 (right). The vertical action was inferred from the oscillation amplitudes in each time window. The amplitude-dependent tune shifts calculated by an off-line model and the measurement agreed to within 5%.

Higher-Order Resonances and Hamiltonian Reconstruction: Nonlinear magnetic fields not only cause a tune shift with amplitude, they also induce higher-order resonances. These show up as additional lines in the Fourier spectrum.

In general, betatron resonances are defined by the condition

$$kQ_x + lQ_y = p \tag{23}$$

where k, l, and p are integers. Spectral analysis in the presence of nonlinear resonances [30] shows that in the Fourier spectrum of the horizontal coordinate $x(n)$, the above resonance gives rise to lines at the two frequencies $(k \pm 1)Q_x + lQ_y$, and in the Fourier spectrum of the vertical signal $y(n)$ it generates lines at $kQ_x + (l \pm 1)Q_y$. Note that there is no line at $kQ_x + lQ_y$, as one might have naively expected! The amplitude and phase of the higher-order resonance lines in the FFT spectrum can be used to reconstruct the nonlinearities affecting the beam motion [31,32].

Tune Scans: The beam lifetime is often related to the dynamic aperture of the storage ring, where the term 'dynamic aperture' denotes the maximum stable betatron amplitude beyond which particles are lost after a certain finite number of turns. In the case of colliding beams, the lifetime is likely limited by the beam-beam interaction. Both dynamic aperture and the beam-beam interaction are sensitive to the value of the betatron tune. Measuring and plotting the beam lifetime as a function of the horizontal and vertical betatron tunes, Q_x and Q_y, yields a tune diagram, in which higher-order resonances, given by Eq. (23), are evident as stripes with reduced lifetime. Figure 8 compares a typical beam-lifetime tune scan performed during the commissioning of the PEP-II High Energy Ring with the result of a dynamic-aperture simulation [33].

4 Betatron Phase

4.1 Harmonic Analysis of Orbit Oscillations

By exciting transverse oscillations, sampling the beam position over N turns, and performing a simple harmonic analysis, we can determine the betatron phase at the location of the pick up [34].

The oscillation detected by the BPM is a harmonic function

$$x_{km} = A_k \cos(2\pi Q_x m + \phi_{0k}) \tag{24}$$

where the index k specifies the BPM, m is the turn number, and A_k the measured amplitude, which depends on the BPM calibration, on the local beta function, and on the magnitude of the oscillation.

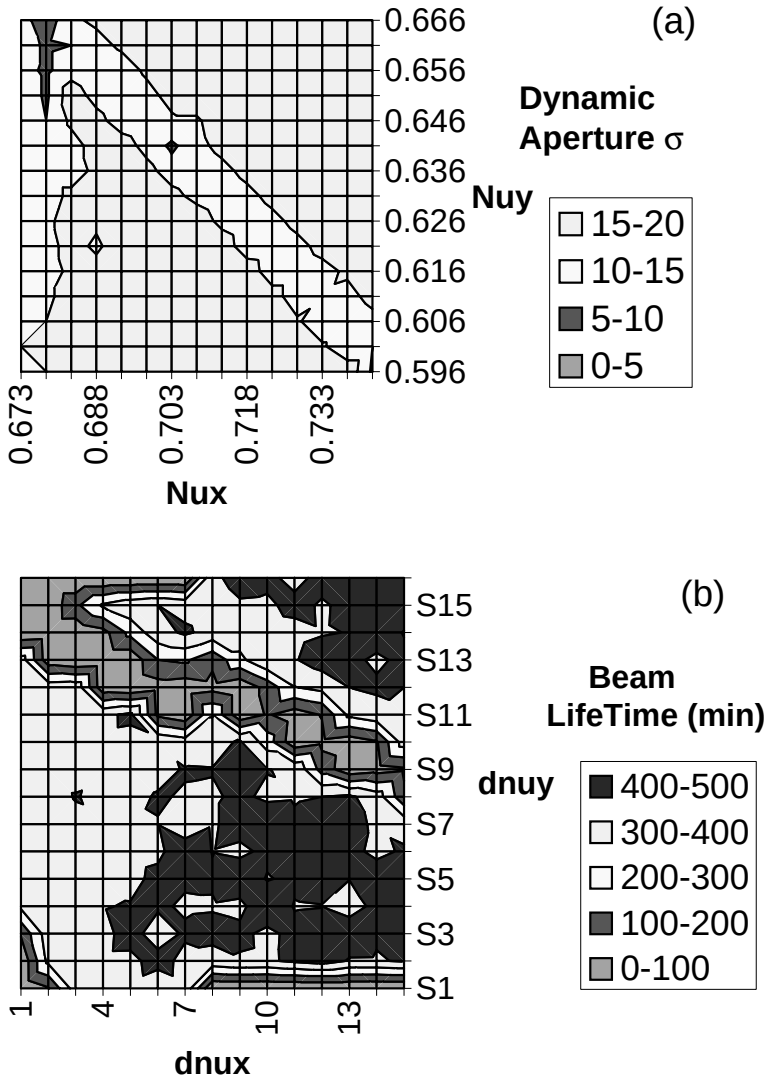

Figure 8: Tune scan in PEP-II centered at $Q_x = 24.709$ and $Q_y = 23.634$[33]: (top) simulated dynamic aperture (for a momentum offset $\Delta p/p = 10\ \sigma_\delta$, where δ is the rms momentum spread) as a function of the horizontal and vertical betatron tunes, Q_x and Q_y; (bottom) measured beam lifetime as a function of Q_x and Q_y. Total scan range is ± 0.005 on both axes. The different slope of the resonance line, as compared with the top figure, is attributed to a miscalibration of the tune knobs. (Courtesy Y. Cai, 1998.)

In the limit of large N, the two Fourier sums

$$C_k = \sum_{m=1}^{N} x_{km} \cos(2\pi m Q_x), \qquad S_k = \sum_{m=1}^{N} x_{km} \sin(2\pi m Q_x). \tag{25}$$

approach the asymptotic values

$$C_k \approx \frac{AN}{2} \cos\phi_{0k} \qquad S_k \approx \frac{AN}{2} \sin\phi_{0k}, \tag{26}$$

and, thus, the betatron phase at the kth monitor can be expressed as

$$\phi_{0k} \approx \tan^{-1}\left(\frac{S_k}{C_k}\right) \tag{27}$$

and the amplitude is given by $A_k \approx 2\sqrt{C_k^2 + S_k^2}/N$. Figure 9 shows 5 consecutive measurements of the betatron phase advance around the PEP-II HER. The phase advance predicted by the model was subtracted from the measured phase. The figure demonstrates that the measurement is highly reproducible, and that, for this example, it is in good agreement with the model. The offset of about 40° is due to different reference points in model and measurement.

Application: Transverse Impedance Measurement

Measuring the betatron phase advance for different bunch currents provides information about the effective transverse impedance, a quantity which describes the electromagnetic coupling of the beam to its environment. A measurement of the current-dependent phase advance around the LEP ring is shown in Fig. 10. Clearly visible as step changes are the locations of the rf cavities in the straight sections.

5 Beta Function

5.1 Tune Shift induced by Quadrupole Excitation

Presumably the simplest beta-function measurement is to detect the shift in the betatron tune as the strength of an individual quadrupole magnet is varied. This shift can be computed using the 'thin-lens' approximation of Eq. (10). The tune shift induced by a gradient change for a long quadrupole can then be obtained by linear superposition.

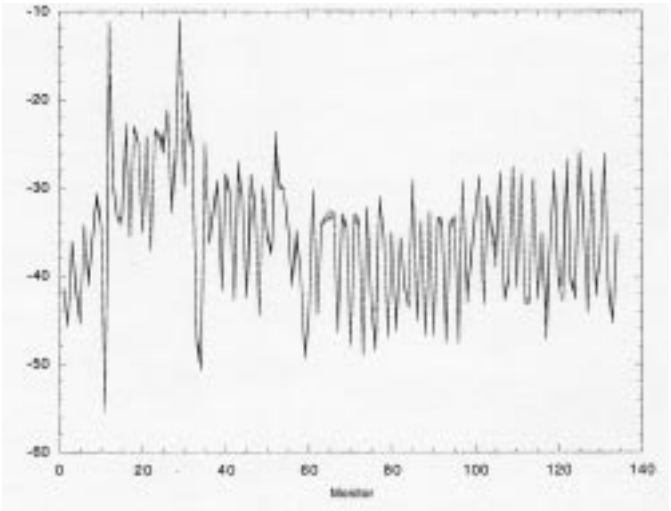

Figure 9: Difference between measured and predicted betatron phase advance (in degrees) as a function of position around the PEP-II HER (BPM number) for 5 consecutive measurements; the 5 curves are superimposed. The total phase advance around the ring is about 9000°. (Courtesy M. Donald, 1998.)

With a quadrupole excitation of Δk, the 2×2 transport matrix for the entire ring is the product of the original transport matrix, Eq. (12) with $f = i$,

$$\begin{pmatrix} \cos(2\pi Q_{x,y}) + \alpha_{x,y}\sin(2\pi Q_{x,y}) & \beta_{x,y}\sin(2\pi Q_{x,y}) \\ -\sin(2\pi Q_{x,y}) & \cos(2\pi Q_{x,y}) - \alpha_{x,y}\sin(2\pi Q_{x,y}) \end{pmatrix}, \quad (28)$$

and a perturbation matrix representing the effect of the change in gradient,

$$\begin{pmatrix} 1 & 0 \\ -(\pm\Delta k) & 1 \end{pmatrix}, \quad (29)$$

where Q_x is the original tune, $\beta_{x,y}$ and $\alpha_{x,y}$ the optical functions at the quadrupole, and the plus or minus sign refers to the horizontal and vertical plane, respectively. The function $\beta_{x,y}$ is to be determined.

The trace of the product matrix must be equal to $2\cos(2\pi\bar{Q}_{x,y})$, where $\bar{Q}_{x,y} = (Q_{x,y} + \Delta Q_{x,y})$ is the new tune, and $\Delta Q_{x,y}$ the tune shift induced by a quadrupole excitation of Δk. Explicit evaluation of the trace gives the equation

$$2\cos(2\pi(Q_{x,y} + \Delta Q_{x,y})) = 2\cos(2\pi Q_{x,y}) - \beta_{x,y}(\pm\Delta k)\ \sin(2\pi Q_{x,y}) \quad (30)$$

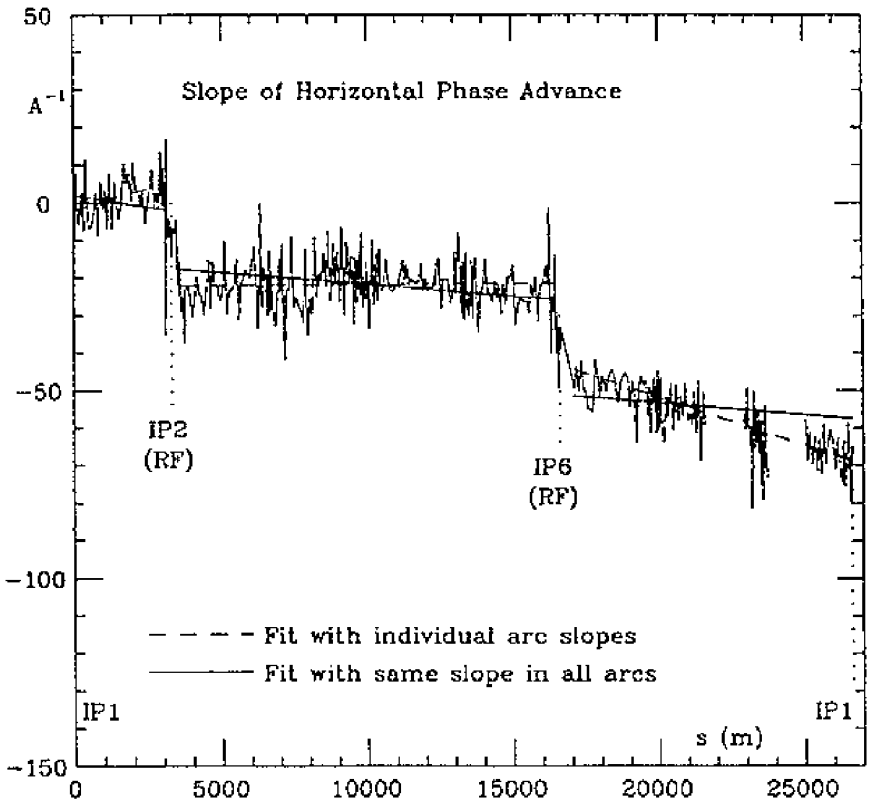

Figure 10: Dependence of the horizontal betatron phase advance on the bunch current, $d\phi/dI_b/(2\pi)$ in units of A^{-1}, measured at LEP [35]. (Courtesy A. Hofmann, 1998.)

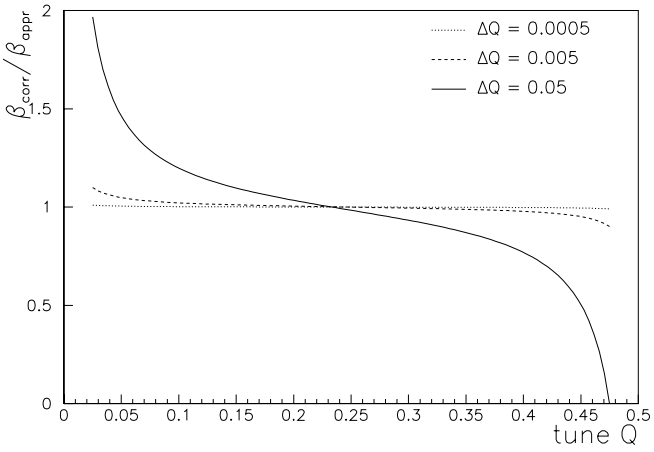

Figure 11: The ratio β_{cor}/β_{appr} of the correct beta function, β_{cor}, inferred from Eq. (31), to the approximation β_{appr} given in Eq. (32), as a function of the nominal tune Q. The three curves correspond to different magnitudes of ΔQ.

Solving for $\beta_{x,y}$ we find [36]:

$$\beta_{x,y} = \pm \frac{2}{\Delta k} \left(\cot(2\pi Q_{x,y}) \left\{1 - \cos(2\pi \Delta Q_{x,y})\right\} + \sin(2\pi \Delta Q_{x,y})\right) \qquad (31)$$

where the $\pm$ sign refers to the horizontal and vertical planes, respectively. For a small tune change, (*i.e.*, $2\pi\Delta Q_{x,y} \ll 1$), far from the integer or half integer resonance (*i.e.*, $\cot(2\pi Q_{x,y}) \leq 1$), we can further simplify and obtain

$$\beta_{x,y} \approx \pm 4\pi \frac{\Delta Q_{x,y}}{\Delta k} \qquad (32)$$

Figure 11 illustrates the error involved in approximating Eq. (31) by Eq. (32). The difference between the two expressions becomes important if $Q_{x,y}$ is close to an integer or half integer resonance, and for large changes Δk [36].

Care also has to be taken that the applied change in quadrupole strength does not alter the beam orbit, which happens if the beam is off-center in the quadrupole whose strength is varied. If the orbit changes, part of the measured tune shift could be caused by the closed-orbit variation at the sextupole magnets elsewhere in the accelerator. If a strong effect on the orbit is observed, the orbit should first be corrected with the help of steering correctors before

the new (shifted) tune value is measured. Sometimes, several magnets are connected to the same power supply, and then the strengths k_i $(i = 1, ..., m)$ of m quadrupoles must be changed simultaneously, all by the same amount Δk. The above result is easily generalized to this case: the induced tune change is related to the average beta function at the m quadrupoles via $< \beta_{x,y} >_m \approx \pm 4\pi \frac{\Delta Q_{x,y}}{m \Delta k}$.

A β function measurement based on the tune shift induced by quadrupole excitations requires independent power supplies (or trim coils, or shunts) for single quadrupoles or groups of quadrupoles, as well as a tune monitor.

5.2 Betatron Phase Advance

A different method determines the beta function from betatron oscillations measured with multi-turn beam position monitors (BPMs): the beta function is calculated from the betatron phase advance between three adjacent BPMs. The betatron phase at each BPM can be obtained with a high precision, using Eqs. (25) and (27)[37]. Since the oscillation amplitude may be subject to calibration errors, it is not used as an input to this calculation. Instead, the computed beta functions can be used to check and correct the BPM calibration.

The first row of the matrix $\mathbf{R}_{fi}$ in Eq. (12) can be rewritten as

$$\tan \phi_{fi} = \frac{R_{12}}{R_{11}\beta(s_i) - R_{12}\alpha(s_i)} \tag{33}$$

where ϕ_{fi} is the phase advance from monitor i to monitor f, and the R_{kl} are transport matrix elements between the same two locations. These matrix elements can be calculated from the geometry of the beam line assuming that the quadrupole magnets located between the BPMs are at their nominal strength. For a set of three BPMs, there are two independent equations of the form (33), which we can solve for the two unknowns α and β[37].

Let us denote the transport matrix from BPM 1 to 2 by $\mathbf{M}$ and the matrix from BPM 1 to 3 by $\mathbf{N}$:

$$\mathbf{M}(1 \to 2) = \begin{pmatrix} m_{11} & m_{12} \\ m_{21} & m_{22} \end{pmatrix} \qquad \mathbf{N}(1 \to 3) = \begin{pmatrix} n_{11} & n_{12} \\ n_{21} & n_{22} \end{pmatrix} \tag{34}$$

and denote by ϕ_{21} and ϕ_{31} the phase advances from BPM 1 to 2, and 1 to 3, respectively. Applying Eq. (33) twice, we arrive at two expressions for the values of α and β at the first BPM[37]:

$$\beta(s_1) = \left(\frac{1}{\tan \phi_{21}} - \frac{1}{\tan \phi_{31}} \right) / \left(\frac{m_{11}}{m_{12}} - \frac{n_{11}}{n_{12}} \right) \tag{35}$$

$$\alpha(s_1) = \left(\frac{n_{11}}{n_{12} \tan \phi_{21}} - \frac{m_{11}}{m_{12} \tan \phi_{31}} \right) / \left(\frac{m_{11}}{m_{12}} - \frac{n_{11}}{n_{12}} \right) \tag{36}$$

An example of beta functions obtained by this method is given in Section 5.4, Fig. 13.

5.3 Orbit Change induced by a Steering Corrector

A simple method to measure the local beta function at a steering corrector magnet with a nearby BPM is to excite the corrector and to detect the orbit change at that BPM[38].

The formula for the closed-orbit distortion $\Delta x_{c.o.}$ induced by a single dipole kick is

$$\Delta x_{c.o.}(s) = \Delta\theta \ \frac{\sqrt{\beta(s)\beta(s_0)}\ \cos(|\phi(s)-\phi(s_0)|-\pi Q)}{2\ \sin\pi Q} + \Delta\theta\ \frac{\eta(s)}{\alpha L} \qquad (37)$$

where s is the location of the BPM and s_0 the location where the kick ($\Delta\theta$) is applied. The last term is a small correction reflecting the change in beam energy induced by a kick at a dispersive location, for constant rf frequency. If the locations s and s_0 are the same, and if we ignore the small correction due to the energy change, the formula simplifies, and the beta function at the BPM-corrector pair can be obtained from

$$\beta_{BPM/cor} \approx 2\ \tan\pi Q\ \frac{\Delta x_{c.o.}}{\Delta\theta} \qquad (38)$$

5.4 Identifying Gradient Errors

Once the beta functions have been measured and a significant difference from the model has been found, the source of the discrepancy must be determined. In most cases, the difference from the model beta function will be a beta beat (an oscillation of the measured beta function around the design beta function at twice the betatron frequency) and the source will be a gradient error in one (or more) of the quadrupole magnets.

A gradient error Δk (in units of m^{-1}) at location s_0 will result in a beta beat of the form

$$\Delta\beta(s) = \frac{\beta(s)\beta(s_0)}{2\sin(2\pi Q)}\ \Delta k(s_0)\ \cos(2|\phi(s)-\phi(s_0)|-2\pi Q) \qquad (39)$$

First Turn Trajectories

A first attempt to find the error may consist in exciting steering correctors (or changing the amplitude of the injection kicker) and fitting first-turn difference

trajectories to an on-line or off-line optics model. The difference of two trajectories measured for different injection amplitudes should match a betatron oscillation predicted by the model.

The parameters of the betatron oscillation can be determined by fitting the difference orbit for a few BPMs to the model. The oscillation so obtained is then propagated along the beam line. It will agree with the measured difference trajectory, until it passes the location of a large gradient error, at which point the propagated betatron oscillation and the measurement will start to disagree. The location of the gradient error thus identified can be confirmed by fitting a betatron oscillation backwards starting in a region further downstream. The fit should begin to deviate from the model at the same point as for the forward fit.

In principle, by analyzing first-turn orbits gross optics errors are easily identified. In practice, it is not always so simple, as beam loss, BPM spray (from lost particles), or kicker noise may corrupt the BPM readings on the first couple of turns.

Closed-Orbit Distortion

A variant of this method is to make use of the fact that, except for the location of the corrector, a closed-orbit distortion for a stored beam has exactly the same pattern as a betatron oscillation. Thus, in much the same manner as for the first turn, the model can be used to fit the change in the closed orbit (with and without corrector excitation) to a betatron oscillation, and then to propagate this oscillation around the ring. Again, the location where a noticable disagreement starts identifies the magnet with a gradient error. The excitation of this magnet can be changed, and the measurement repeated, until the agreement with the model is satisfactory. Figure 12 shows an example of this method from the PEP-II commissioning. A gradient error close to the interaction point was clearly identified.

It is possible to considerably extend this simple closed-orbit distortion scheme. For example, the response of all BPMs to every single steering corrector may be combined into a big matrix, which can be used as an input to a sophisticated statistical fitting program, such as LOCO [42,43]. LOCO then varies the individual gradients of the quadrupoles in a computer model (*e.g.*, MAD [44]) to find the gradients that best reproduce the measured orbit response data.

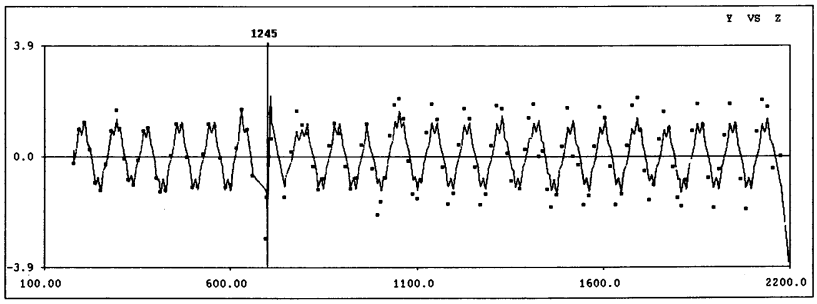

Figure 12: Finding quadrupole gradient errors by fitting betatron oscillations to closed-orbit distortions: an example from the PEP-II HER commissioning, using the codes LEGO [40] and RESOLVE [41]. The induced orbit change is fitted to a betatron oscillation over a small number of BPMs (further to the left); the betatron oscillation so obtained is propagated along the beam line using the model optics (solid line) and compared with the actual orbit variation (plotting symbols). In this example, the two agree well up to a region close to the interaction point, near $s = 700$ m on the horizontal axis. It was later verified that two quadrupole pairs in this region had gradient errors of the order of 0.1%. (Courtesy Y. Cai, 1998.)

Phase Advance

Instead of fitting trajectories, we can also use Eq. (35) to compute the beta functions from the measured phase advance around the ring. Then we can adjust either the model quadrupoles or change the actual magnet settings of the machine to improve the agreement of measured and predicted phase advance and to identify the source of the discrepancy.

An example from PEP-II is presented in Fig. 13 [45]. From left to right we see the improved agreement of model and measurement, when the strength of a quadrupole pair (QF5) in the IP region is changed by a total of 0.15%. For each quadrupole value, the upper row of pictures shows the entire ring, the lower row a close-up view of a particular section. As can be seen, the final quadrupole strength, on the right, yields a satisfactory agreement with the model.

π Bump Method

Another method which can be used to identify local gradient errors is the π-bump technique, applied at Tristan and at the ATF [46,47,48]. Here, local orbit bumps are induced, one by one, across each quadrupole magnet (or across small groups of quadrupole magnets), so as to cover the entire ring. The non-closure of a theoretically closed bump is indicative of an optics error in this region. Of

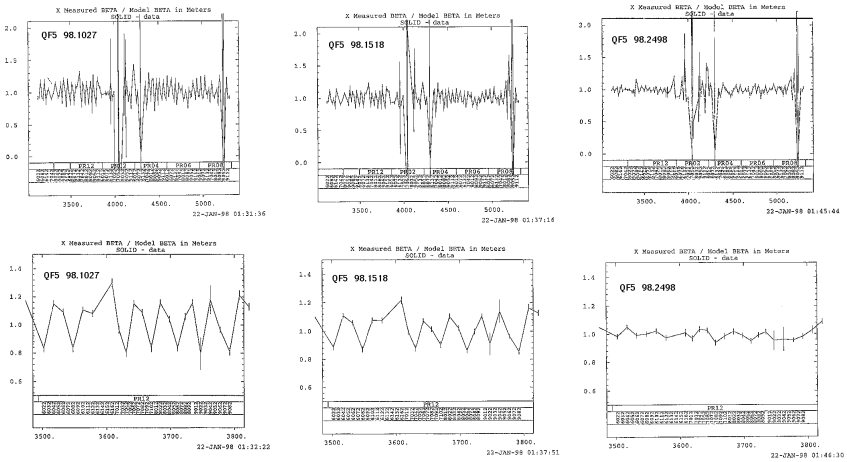

Figure 13: Ratio of the horizontal beta function inferred from phase advance measurements to the model beta function: (top row) for the entire PEP-II High Energy Ring (HER); (bottom row) for a limited region only; (left column) with all magnets at nominal strength; (center) for an increased strength of a single quadrupole pair (called QF5) by 0.1%; (right column) for a strength increase of 0.15%. The fliers with large error bars correspond to bad BPMs or to a phase advance between successive BPMs equal to 0 or π. (Courtesy M. Donald, 1998.)

course, also an error in the calibration of the bump dipole magnets may result in non-closure of the bump, but the effects of dipole errors and optics errors can be separated by their betatron phase. In particular, for an ideal π bump, the bump leakage due to a gradient error and that due to a dipole error are perpendicular to each other. In more complex situations, computer programs can be used to process a large number of measurements for overlapping bumps, so as to determine both the dipole and the focusing errors.

5.5 β^* at Interaction or Symmetry Point

To determine the beta function at the interaction point of a collider ring, or at any other symmetry point (*e.g.*, in a light source), one can excite a pair of symmetrically placed quadrupoles, by an amount $\pm\Delta k$ (asymmetric excitation), where k is the integrated quadrupole gradient in units of m^{-1}. From Eq. (32), the total tune shift is given by

$$\Delta Q_{tot} = \Delta Q_+ - \Delta Q_- \approx \frac{\Delta k}{4\pi} \left[< \beta_+ > - < \beta_- > \right] \tag{40}$$

where $< ... >$ indicates the average over the quadrupole, and the $\pm$ sign refers to the left or right quadrupole. The advantage of the asymmetric excitation of two quadrupoles is that, if the phase advance between the two quadrupoles is about 180 degree, almost no beta beat is induced. In addition, if the optics is perfect and the beam waist is centered at the collision (or symmetry) point, the beta functions at the two quadrupoles are the same and, to first order, there is no net tune change $\Delta Q_+ - \Delta Q_- = 0$.

The beta function at the collision (symmetry) point β^* is a quadratic function of the ratio

$$\eta = < \beta_+ > - < \beta_- > = 4\pi \, \frac{\Delta Q_+ - \Delta Q_-}{\Delta k} \tag{41}$$

which takes the form [49]

$$\beta^* = \beta^*_{design} \left(1 + a_{optics} \eta^2 \right) \tag{42}$$

where β^*_{design} is the nominal interaction-point beta function, and the coefficient a_{optics} depends on the optics between the quadrupoles which are being varied and the interaction point, and can be calculated with any optics program, *e.g.*, MAD [44]. For the LEP low-β insertions, $a_{optics} \approx 1/15$ [49]. The optics is perfectly adjusted, if $\Delta Q_{tot} = 0$.

5.6 R Matrix from Trajectory Fit

Consider a set of three BPMs, which are not a multiple of π apart in betatron phase and with nonzero dispersion for at least one. The horizontal orbit readings at these three BPMs, $x^{(1)}$, $x^{(2)}$, and $x^{(3)}$, then contain complete information about the betatron motion (x and x') and the energy offset (δ) of each trajectory. This means we can express the orbit at every other BPM as a linear combination of the orbit reading for these three BPMs:

$$x(s) = B(s)x^{(1)} + C(s)x^{(2)} + D(s)x^{(3)} \tag{43}$$

If the three BPMs are adjacent, and the optics between them is known, Eq. (43) is equivalent to the more familiar form,

$$x(s) = R_{11}^{s_0 \to s} x(s_0) + R_{12}^{s_0 \to s} x'(s_0) + R_{16}^{s_0 \to s} \delta, \tag{44}$$

because then the three variables $x(s_0)$, $x'(s_0)$ and δ are known linear combinations of $x^{(1)}$, $x^{(2)}$ and $x^{(3)}$.

If we take data sets for many different turns (in a ring) or for many bunch passages (in a transport line), we can obtain the coefficients $B(s)$, $C(s)$, and $D(s)$, or equivalently the R matrix elements R_{11}, R_{12} and R_{16}, by a fitting procedure. However, care has to be taken: a simple least squares fit may not give the right answer. The reason is that the BPM readings on the left and right side of Eq. (44) both have a noise component.

The effect of the noise in the horizontal coordinates can be illustrated by a simple example, taken from Ref. [50]. We consider a linear fit of the form $y = px + q$, where p and q are to be determined, and both x and y are smeared stochastically. Figure 14 shows the reconstructed slope normalized to the true slope as a function of the signal to noise ratio in the horizontal coordinate, R_x. Even for a signal-to-noise ratio of 3 the fitted slope still has a 10% error. This result is independent of the noise in the y coordinate.

A better approach, which takes into account the noise in the horizontal coordinates, is schematically to 'find the principal axes of the set of data points and then turn the parameter vector parallel to the principal axis along which the data points fluctuate the least' [50]. The general problem and its solution are as follows. Let x_n be a measured variable which is linearly correlated with $(n-1)$ other measurements $x_1, ..., x_{n-1}$, and suppose there are a total of N data sets. We introduce normalized coordinates:

$$z_i = \frac{x_i - < x_i >}{\sigma_i} \tag{45}$$

Using these coordinates, the fit equation (43) or (44) is rewritten as

$$\mathbf{u}^T \cdot \mathbf{z} = 0 \tag{46}$$

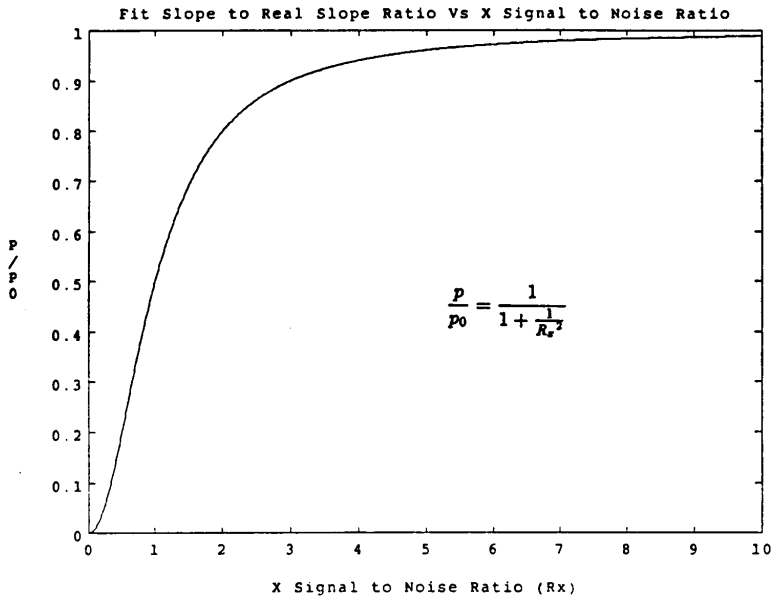

Figure 14: Systematic slope error introduced in a linear χ^2 fit of the form $y = px + q$, neglecting the noise smearing in the x measurement[50]. Shown is the reconstructed slope normalized to the true slope as function of signal-to-noise ratio R_x in the horizontal coordinate. (Courtesy P. Emma, 1998.)

Introducing the symmetric covariance matrix

$$C_{ij} = \sum_{l=1}^{N} z_{li} z_{lj} \tag{47}$$

Eq. (46) is solved in a least squares sense by

$$\mathbf{C} \cdot \mathbf{u} = \lambda u \tag{48}$$

$$|\mathbf{u}|^2 = 1 \tag{49}$$

$$\chi^2 = \lambda \tag{50}$$

where the solution $\mathbf{u}$ is simply the normalized eigenvector corresponding to the smallest eigenvalue λ of $\mathbf{C}$; λ is also the χ^2 of the fit.

If we assume that $\lambda = \lambda_1$ (the smallest eigenvalue) is not degenerate, and cosider a scalar function $f(\mathbf{u})$ of the fit parameters $\mathbf{u}$, the rms fit error in f is given by

$$\sigma(f)^2 = (\nabla_{\mathbf{u}} f)^T \cdot \mathbf{T} \cdot (\nabla_{\mathbf{u}} f) \tag{51}$$

where $\mathbf{T}$ is a symmetric $n \times n$ matrix defined by

$$T_{ij} = \sum_{r=2}^{n} \frac{\lambda_r + \lambda}{(\lambda_r - \lambda)^2} \, (u_r)_i (u_r)_j \tag{52}$$

In particular, the rms error of the coefficient u_i in the normalized equation (46) is simply $\sigma(u_i) = \sqrt{T_{ii}}$.

The reconstruction of lattice parameters from orbit and energy fluctuations can be studied by computer simulations. Figure 15 presents simulation results for the SLC final focus with an assumed BPM resolution of 20 μm, employing both a standard χ^2 fit and a principal axes transformation. The results of the former differ strongly from the underlying model parameters, despite of good fits and small error bars, while the principal axes method reconstructs the optics almost perfectly.

5.7 R Matrix Reconstruction from Induced Ocillations

The approach of the previous section was to measure the lattice parameters by correlating BPM data of natural orbit fluctuations, with a moderate signal-to-noise ratio. The lattice can also be reconstructed by introducing a series of large betatron oscillations and measuring the response of the BPM readings to these perturbations [51]. The betatron oscillations are induced by stepping the strengths of a set of dipole correctors, located at different betatron phases,

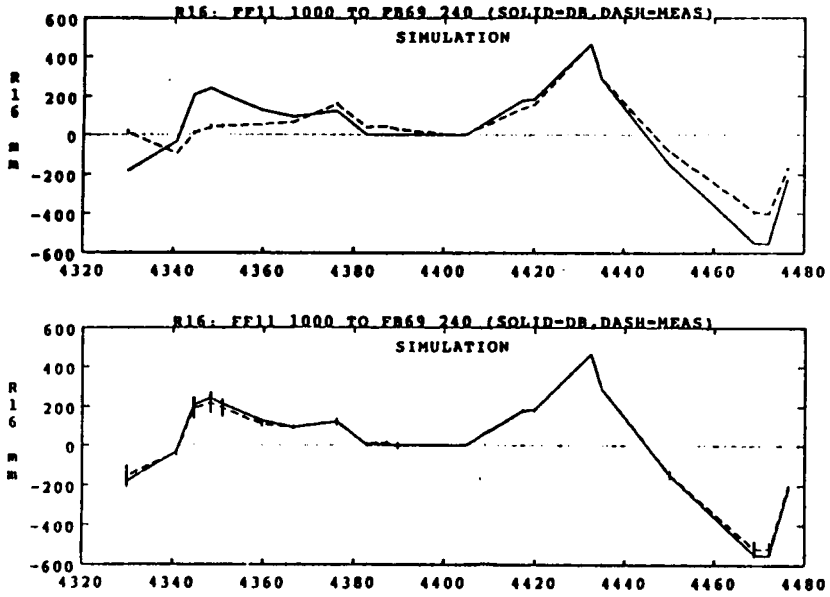

Figure 15: Reconstructed final focus R matrix element R_{16}, from a sample of 100 simulated trajectories with fluctuations in betatron orbit and energy, and assuming 20 μm BPM resolution [50]: (top) standard χ^2 fit; (bottom) principal axes transformation. The fit results (dashed) are compared to the model used for the trajectory generation (solid). (Courtesy P. Emma, 1998.)

over several increments and to record the BPM readback for each corrector setting. The resulting BPM responses are then fitted to obtain an estimate of the R_{12} transport matrix elements between the correctors and the BPMs, as well as their errors. If the dispersion at the BPMs is nonzero, the beam energy for each measurement should be determined as well and be included in the analysis.

Assuming the linear transport matrices between the different correctors and the transport matrices between every 4 adjacent BPMs are known with sufficient accuracy, the R matrix between the correctors and the BPMs can be determined by a simple least squares fit[51]. Including the additional constraint that the R matrix has to be symplectic eliminates several degrees of freedom, but then the problem must be solved by non-linear regression[51].

Reference[51] describes how a rigorous error analysis allows an estimate of the unknown systematic errors.

5.8 Beta Matching in a Transport Line or Linac

The beta functions in a transport line (or linac) depend on the incoming beam parameters. To match the beam line optics to the incoming beam, two procedures are frequently used: multi-wire (or multi-screen) emittance measurements and quadrupole scans. Both methods are based on wire scanners or screen monitors measuring the transverse beam size. The beam size (squared) at the location s can be expressed in terms of the α and β functions and the emittance at an upstream location s_0 as

$$< x^2(s) >= R_{11}^2\beta(s_0)\epsilon - 2R_{12}R_{11}\alpha(s_0)\epsilon + R_{12}^2\gamma(s_0)\epsilon \qquad (53)$$

In a quadrupole scan, the transfer matrix elements R_{11} and R_{12} are varied, by changing the strength of a quadrupole between s_0 and s. Beam-size measurements for at least 3 different quadrupole settings are required in order to solve for the three independent unknown parameters: ϵ, $\beta(s_0)$ and $\alpha(s_0)$. The fourth parameter, $\gamma(s_0)$ is not free, but determined by $\alpha(s_0)$ and $\beta(s_0)$: $\gamma = (1+\alpha^2)/\beta$.

A multi-wire (or multi-screen) emittance measurement is very similar. Here, the quadrupole gradients stay constant, but the R matrices between s_0 and the different wire scanners (or other beam-size monitors) are different. Again, at least 3 measurements are required.

Either case can be described by a matrix equation of the form:

$$\begin{pmatrix} \sigma_x^{(1)2} \\ \sigma_x^{(2)2} \\ \sigma_x^{(3)2} \\ \cdots \\ \sigma_x^{(n)2} \end{pmatrix} = \begin{pmatrix} R_{11}^{(1)2} & -2R_{11}^{(1)}R_{12}^{(1)} & R_{12}^{(1)2} \\ R_{11}^{(2)2} & -2R_{11}^{(2)}R_{12}^{(2)} & R_{12}^{(2)2} \\ R_{11}^{(3)2} & -2R_{11}^{(3)}R_{12}^{(3)} & R_{12}^{(3)2} \\ \cdots & & \\ R_{11}^{(n)2} & -R_{11}^{(n)}R_{12}^{(n)} & R_{12}^{(n)2} \end{pmatrix} \begin{pmatrix} \beta(s_0)\epsilon \\ -\alpha(s_0)\epsilon \\ \gamma(s_0)\epsilon \end{pmatrix} \tag{54}$$

where the superindex on the right hand-side refers to the different measurements, *i.e.*, it either corresponds to the setting of some quadrupole magnet, in case of a quadrupole scan, or to a different wire scanner or monitor, in case of a multi-wire emittance measurement. At least 3 measurements are required ($N \geq 3$) in order to solve for the three independent parameters ϵ, $\beta(s_0)$ and $\alpha(s_0)$.

To simplify the notation, let us denote the $n \times 3$ matrix on the right-hand side of Eq. (54) as $\mathbf{B}$, the n-component vector on the left side by $\mathbf{\Sigma}_x = (\sigma_x^{(1)2}, ..., \sigma_x^{(n)2})$, and the 3-component vector on the far right by

$$\mathbf{o} = (\beta(s_0)\epsilon, -\alpha(s_0)\epsilon, \gamma(s_0)\epsilon). \tag{55}$$

The equation then reads:

$$\mathbf{\Sigma}_x = \mathbf{B} \cdot \mathbf{o} \tag{56}$$

The problem of determining the elements of the vector $\mathbf{o}$ can be solved by a simple least-squares fit. We have to minimize the sum

$$\chi^2 = \sum_{l=1}^{n} \frac{1}{\sigma^2_{\Sigma_x^{(l)}}} \left(\Sigma_x^{(l)} - \sum_{i=1}^{3} B_{li} o_i \right)^2 \tag{57}$$

where $\sigma_{\Sigma_x^{(l)}}$ denotes the rms error of $\Sigma_x^{(l)} = \sigma_x^{(l)2}$. This error is obtained from the fit to the lth wire scan which determines the rms beam size $\sigma_x^{(l)}$.

We find it convenient to normalize the coordinates $\Sigma^{(l)}$ so that the rms error is 1:

$$\hat{\Sigma}_x^{(l)} = \frac{\Sigma_x^{(l)}}{\sigma_{\Sigma_x^{(l)}}} \tag{58}$$

$$\hat{B}_{li} = \frac{B_{li}}{\sigma_{\Sigma_x^{(l)}}} \tag{59}$$

Forming a symmetric $n \times n$ covariance matrix

$$\mathbf{T} = (\hat{\mathbf{B}}^T \cdot \hat{\mathbf{B}})^{-1} \tag{60}$$

the least-squares solution to Eq. (56) reads:

$$\mathbf{o} = \mathbf{T} \cdot \hat{\mathbf{B}}^T \cdot \hat{\mathbf{\Sigma}}_x^{(l)} \tag{61}$$

and the error of any scalar function $f(\mathbf{o})$ is given by

$$\sigma(f)^2 = (\nabla_{\mathbf{o}} f)^T \cdot \mathbf{T} \cdot (\nabla_{\mathbf{o}} f). \tag{62}$$

In particular, the errors of the parameters $\mathbf{o}$ themselves are

$$\sigma_{o_i} = \sqrt{T_{ii}} \tag{63}$$

Once the components of $\mathbf{o}$ are known, we still need to perform a simple nonlinear transformation to infer ϵ, β, and α:

$$\epsilon = \sqrt{o_1 o_3 - o_2^2} \tag{64}$$

$$\beta = o_1/\epsilon \tag{65}$$

$$\alpha = -o_2/\epsilon \tag{66}$$

The error propagation is straightforward, using Eq. (62).

The deviation of the β, α, and γ from the design parameters β_0, α_0 and γ_0 is often characterized in terms of a so-called 'Bmag' (β matching) parameter [52,53]:

$$\text{Bmag} = \frac{1}{2}\ (\beta\gamma_0 - 2\alpha\alpha_0 + \gamma\beta_0) \tag{67}$$

The parameter Bmag has an important physical meaning. If a beam is injected into a ring or linac with a mismatch, the beam will filament until its distribution approaches a shape that is matched to the ring or the linac lattice. However, the filamentation causes the beam emittance to increase, such that, after complete filamentation, the emittance is given by the product of Bmag and the initial value of ϵ.

Once the values of β and α are known, quadrupole magnets can be adjusted so as to match the optical functions at a selected point to their design value, which is equivalent to Bmag=1. The above procedure also provides an absolute measure of the emittance. The SLC has more than 10 multi-wire emittance measurement stations, which monitor the beam emittances in various parts of the machine in hourly intervals, and are indispensable for emittance control and tuning. For example, in the SLC linac transverse orbit bumps are intentionally induced as a global correction which cancels the accumulated local effects of dispersion or wakefields. The bumps are optimized by minimizing the emittance downstream, as calculated by this measurement technique.

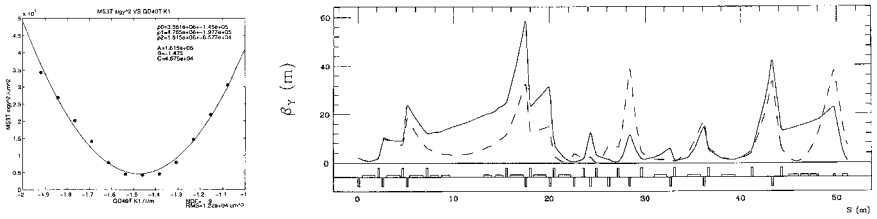

Figure 16: Beta matching in the KEK/ATF BT [54]: (left) quadrupole-scan emittance measurement; shown is the square of the vertical beam size on a profile monitor vs. the strength of an upstream quadrupole; (right) the vertical beta function obtained by propagating the measured twiss parameters (solid) through the actual BT optics is compared with the beta function expected for the design optics (dashed). (Courtesy R. Iverson, M. Minty, M. Woodley, 1998.)

Example

To illustrate the beta matching method, Fig. 16 shows an example from the KEK/ATF beam transport line (BT), connecting the S-band linac and the ATF damping ring. The left picture shows the result of a typical quadrupole scan at the end of the BT. Plotted is the square of the vertical beam size versus the strength of an upstream quadrupole, as well as a quadratic fit to the data. We can propagate the twiss parameters deduced from such a fit through the BT, using a model derived from the actual or the design magnet settings. The right picture displays the inferred beta functions.

5.9 Injection Envelope Matching

At injection into a storage ring, if the incoming beam distribution is not properly matched to the ring optics, the beam envelope in phase space will rotate around the matched design envelope. This oscillation will result in turn-to-turn beam-size variations, which can be measured on a synchrotron light monitor using a gated camera.

An injection-mismatch measurement from the SLC damping ring [55,56] is shown in Fig. 17. The different pictures correspond to successive turns after injection, starting with turn number one. Each picture is an average over 8 individual images. Clearly visible is a variation of the bunch shape from turn to turn.

In case of the SLC damping ring, the matching of the injected beam distribution consists of minimizing the measured beam size after 1250 turns, by varying several quadrupoles at the end of the injection beam transport line.

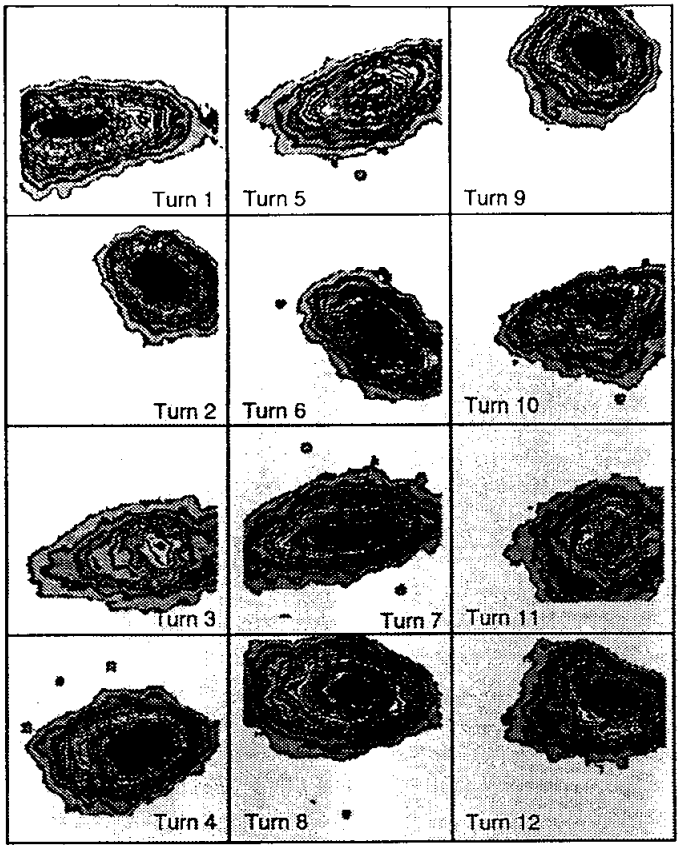

Figure 17: Beam images on the first twelve turns after injection into the SLC Damping rings, illustrating the effect of an injection mismatch[55,56]. These are pictures from a synchrotron light monitor taken with a gated camera. Each image is an average over 8 beam pulses. The beam-size variation from turn to turn is an indication of injection mismatch. (Courtesy M. Minty, 1998.)

A number of 1250 turns was chosen, because at this time the initial beta and dispersion mismatch has completely filamented, and, since the time scale is much shorter than the radiation damping time, the emittance is given directly by Bmagϵ, where ϵ is the emittance of the injected beam.

It is interesting to note that, in much the same manner as for the centroid motion measured with BPMs, the beam size variation can be analyzed in the frequency domain by a Fourier transform. A beta mismatch will appear as a frequency line at twice the betatron tune, while a dispersion mismatch will be evident as a line at the betatron tune itself[56]. If only a beta mismatch is present, the ratio ρ of the dc Fourier component and the component at $2Q_x$ is equal to (Bmag/$\sqrt{\text{Bmag}^2 - 1}$). From this, Bmag $= 1/\sqrt{1-\rho^{-2}}$ can be determined[56,52].

Figure 18 shows the beam size for the first 100 turns after injection, as well as the FFT (multiplied with γ/β). Clearly visible are peaks at $2Q_x$ in the horizontal signal and at $(1-2Q_y)$ in the vertical one. The final emittance after filamentation, Bmagϵ, is given by the dc component of the FFT.

The matching procedure applied reduces the FFT signals at $2Q_x$, $(1-2Q_y)$ and Q_x, as illustrated in Fig. 19.

6 Beam-Based Alignment

In many modern accelerators, the alignment tolerances on quadrupole and sextupole magnets are so tight that they cannot be achieved by state-of-the art surveying and installation methods with residual errors of 100-200 μm. The standard approach to achieve and maintain tight tolerances is beam-based alignment.

What matters is the relative alignment of the beam and the magnets. If the beam passes off center through a quadrupole, it receives a dipole kick. The steering thus induced can put the beam off center in subsequent sextupoles, thereby changing the optics. If a beam is horizontally off center in a sextupole magnet, the sextupole adds an additional quadrupole field; if the displacement in the sextupole is vertical, skew coupling is introduced. In addition, the kick from the displaced quadrupole is energy-dependent, and the orbit change downstream may also be energy dependent if the chromaticity is not zero, generating dispersion. All of these effects cause emittance dilution. At a future linear collider, such dilutions will increase the spot size at the collision point, while, in a light source or damping ring, they will increase the vertical equilibrium emittance. It is thus highly desirable to steer the beam through the center of the quadrupole magnets. As an additional benefit, also the orbit motion induced by quadrupole power-supply instability is minimized when

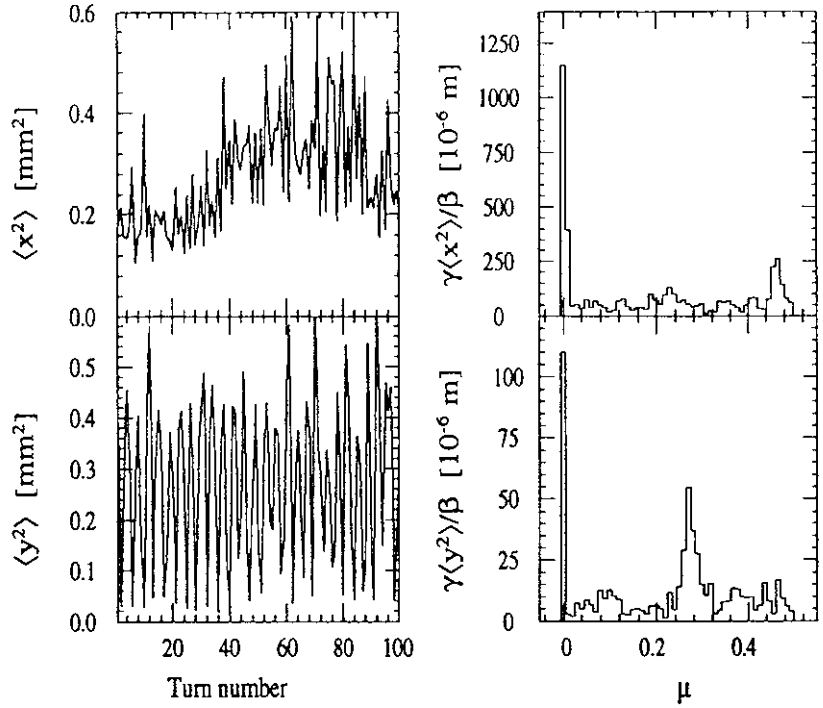

Figure 18: Horizontal (top) and vertical (bottom) beam sizes for the first 100 turns after injection into the SLC damping ring (left) and their FFT (right) [56]. Clearly visible in the frequency spectra are lines at $2Q_{x,y}$ (top) and at $1 - 2Q_y$ (bottom), whose amplitude is a measure of the amount of beta mismatch. (Courtesy M. Minty, 1998.)

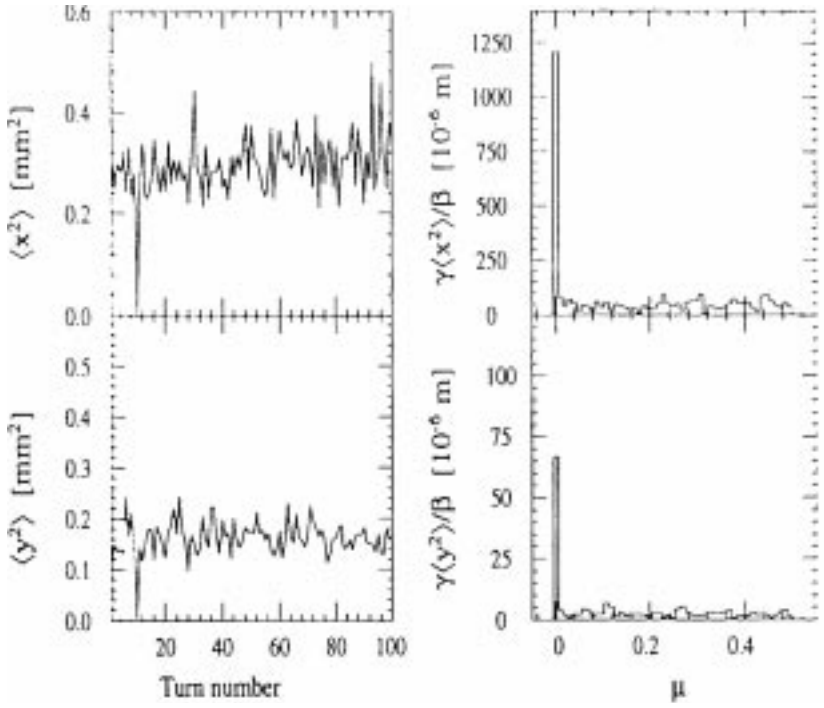

Figure 19: Same as Fig. 18, after beta matching [56]. The peaks at twice the betatron tune have disappeared. (Courtesy M. Minty, 1998.)

the beam passes through the magnetic center. It is further noteworthy that random orbit kicks in the vertical plane due to quadrupole misalignments can cause depolarization in electron storage rings, and that beam-based alignment can significantly increase the equilibrium polarization[57,58]. Finally, in a linac, not only magnets but also the accelerating structures must be aligned with respect to the beam to avoid emittance growth or beam break up caused by transverse wakefields.

Beam-based alignment determines the relative offset between magnet centers and nearby BPMs. If these offsets are sufficiently stable, a simple orbit correction (steering) can maintain a well-centered orbit, until the alignment measurement is repeated at a later time (after several months).

6.1 Quadrupole Excitation

If the beam is not centered in a quadrupole magnet, and the strength of this quadrupole is varied, the beam receives a kick. This causes a change in the beam trajectory, for single-turn measurements, or a change in the closed orbit, for measurements on a stored beam.

For a single-pass measurement, the dipole kick θ can easily be inferred by fitting the difference trajectory to a betatron oscillation including one additional kick at the location of the quadrupole. The dipole kick θ obtained from the fit is proportional to the quadrupole misalignment x_q and the change in the integrated quadrupole strength:

$$\theta = \Delta k \; x_q \tag{68}$$

If beam-based alignment is performed on a stored beam, the additional kick of the closed orbit induced by the change in quadrupole strength is given by the sum of two components, the change in field strength and the change in the closed-orbit offset at the quadrupole. In lowest order, we have[59]

$$\theta \approx \Delta k \; x_q - k \; \Delta x \tag{69}$$

where x_q is the original quadrupole offset, Δx the change in closed-orbit position, k the integrated quadrupole gradient, and we have neglected a second-order term ($\Delta k \; \Delta x$). We can apply the formula for the closed orbit distortion at the location of the dipole kick, Eq. (38), and find

$$\Delta x = (\Delta k \; x_q - k \; \Delta x) \; \left(\frac{\beta}{2 \tan \pi Q} \right) \tag{70}$$

which we can solve for Δx,

$$\Delta x = \Delta k \; x_q \left(\frac{\beta/(2 \tan \pi Q)}{1 + k\beta/(2 \tan \pi Q)} \right) \tag{71}$$

Inserting this back into Eq. (69) gives the closed-orbit kick induced by a gradient change Δk:

$$\theta = \Delta k \; x_q \left(\frac{1}{1 + k\beta/(2 \tan \pi Q)} \right). \tag{72}$$

This is the stored-beam equivalent of Eq. (68).

The precision of this method is very much improved by taking difference orbits for several quadrupole-to-beam off-sets, Δx_q, varied with a local bump [57]. One can also define a merit function

$$f(\Delta x_q) = \frac{1}{N_{BPM}} \sum_{i=1}^{N_{BPM}} (x_i(\Delta k) - x_i(-\Delta k))^2, \tag{73}$$

where N_{BPM} is the total number of BPMs in the ring, and determine the quadrupole offset by minimizing $f(\Delta x_q)$ as a function of the bump amplitude Δx_q, using a least-squares parabolic fit. At the Advanced Light Source (ALS), this procedure measures the center of the quadrupoles to within ± 5 μm [59] (in case of the ALS, the orbit at the quadrupole is varied with a single corrector and not by a closed bump).

This type of measurement does not require an independent power supply for each quadrupole to be aligned, but, for several magnets in series, a simple switchable shunt resistor across each magnet will suffice. Simultaneously, such shunt resistors allow a measurement of the beta function, via Eq. (32).

Figure 20 illustrates the application of this technique at the storage ring SPEAR. The left figure shows the circuit diagram for a magnet with shunt resistor, and the right figure presents a typical alignment measurement for a SPEAR quadrupole. Plotted in the right figure is the orbit shift induced by the shunt at two downstream BPMs as a function of the orbit at the shunted quadrupole, which is varied by a local bump. The orbit is centered in the quadrupole when no orbit shift is induced by the shunt (the intersection of the two lines).

If the number of BPMs is small and only groups of quadrupoles can be changed simultaneously, it is still possible to determine the quadrupole misalignments, by applying a statistical fit to a sufficiently large number of trajectories taken for different quadrupole-group excitations, different incoming conditions and different corrector settings. An interesting example of such an analysis can be found in Ref. [61].

6.2 Quadrupole Gradient Modulation

A scheme which allows continuous monitoring of quadrupole alignment and BPM offsets was implemented at LEP; see, *e.g.*, Ref. [62]. Here the strength of

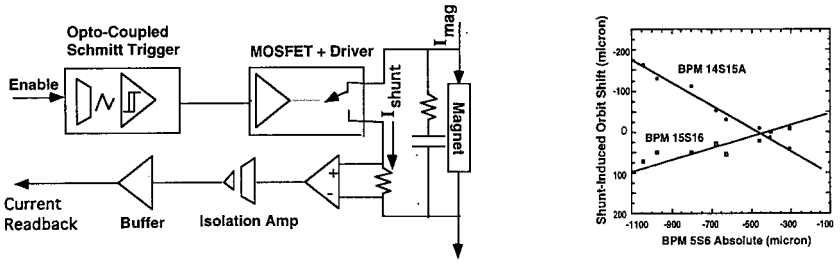

Figure 20: Beam-based alignment with quadrupole shunts at SPEAR [60]: (left) electric circuit with shunt resistor; (right) shunt-induced orbit shift at two downstream BPMs as a function of the beam-position read back at the BPM nearest to the quadrupole being varied. (Courtesy J. Corbett, 1998.)

several quadrupoles is modulated at different frequencies in the range 0.8-15.6 Hz, and the induced oscillation amplitude, of the order of 1 μm is detected. Figure 21 shows the FFT over 4096 data points of this detector signal, at a time when four quadrupoles were modulated. Clearly visible are 4 peaks in the frequency sprectrum, corresponding to the four different modulation frequencies. The amplitude of the peak is proportional to the beam offset in that quadrupole.

Using this k modulation technique, one can infer the BPM offsets from the naturally occurring beam-orbit jitter and orbit variation. This is illustrated in Fig. 22. The left figure shows a BPM orbit reading in LEP during several hours of a luminosity run. The reasons for the slow changes are not fully understood; the fast steps reflect corrections of the closed orbit. Making use of this natural orbit variation, one can plot the amplitude of the beam response to the quadrupole modulation as a function of the BPM reading for the corresponding quadrupole. The result is a 'V plot', as shown in the right figure. The minimum in this plot determines the BPM reading at which the beam is centered in the quadrupole.

6.3 Sextupole Excitation

In present-day storage rings, it is often assumed that the sextupoles are well enough aligned with respect to the quadrupoles that only the quadrupole alignment has to be verified. An orbit off center in a sextupole will result in vertical dispersion, betatron coupling, or beta beating. Although, in principle, also the sextupoles in a storage ring can be aligned by changing their strength and measuring the induced orbit shift (which is a quadratic function of the excitation)

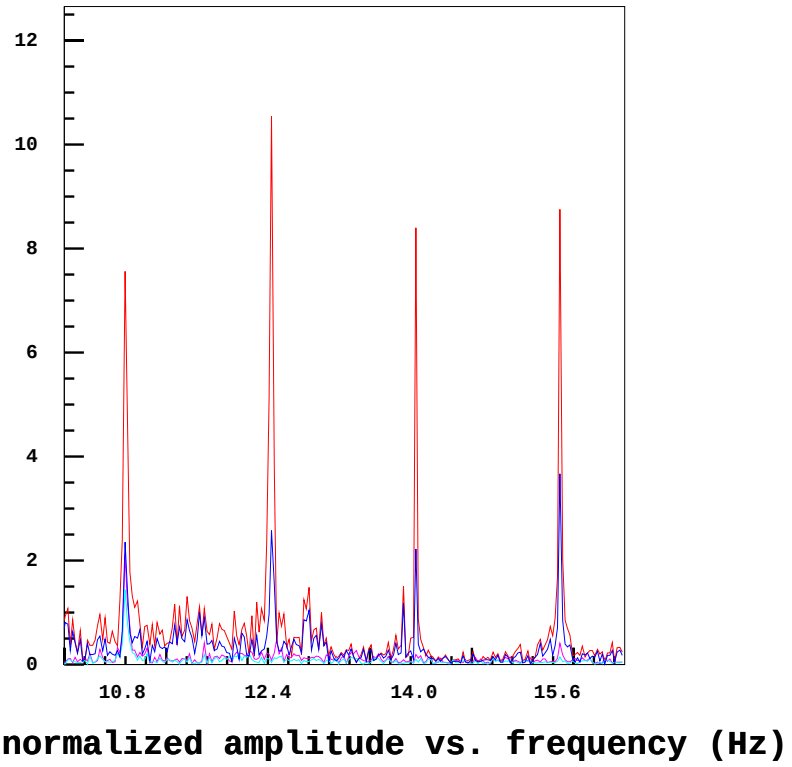

Figure 21: FFT spectra with 4 modulated quadrupoles in LEP [62]. The amplitude of the peaks is proportional to the beam displacement in the 4 quadrupoles. (Courtesy I. Reichel, 1998.)

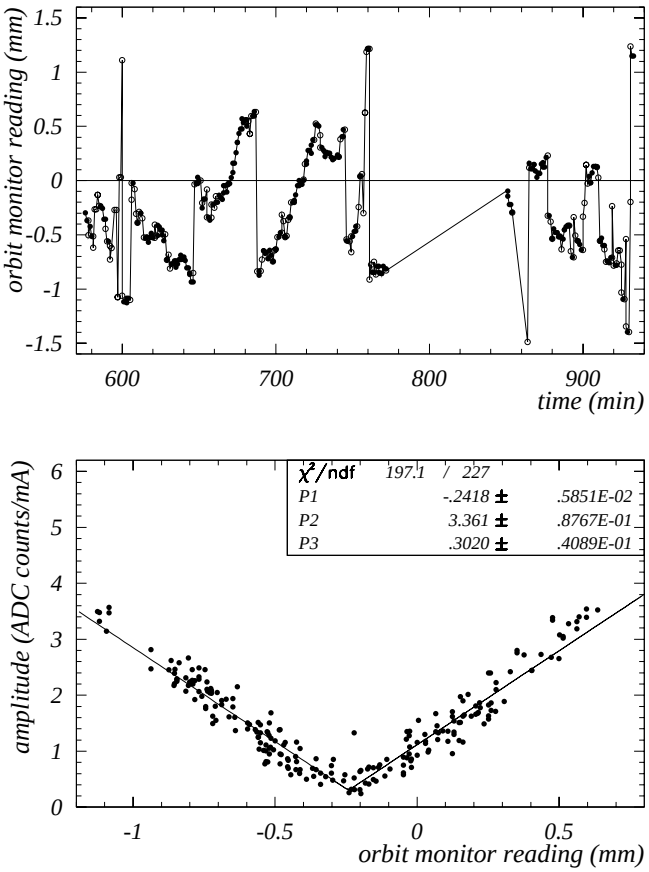

Figure 22: Determination of BPM offsets using k modulation and natural orbit variation in LEP [62]: (top) natural orbit drifts and corrections during a LEP luminosity run at one quadrupole; (bottom) amplitude of beam response to k modulation vs. BPM orbit reading for the modulated quadrupole. The minimum of this plot gives the BPM offset. These data were taken continuously during 5 hours of luminosity run. (Courtesy I. Reichel, 1998.)

there is little experience with such a scheme. To reach the same sensitivity as for the equivalent quadrupole alignment, the change in the sextupole gradient Δk_s would have to be equal to

$$\Delta k_s = \frac{\Delta k_q}{2x_s} \tag{74}$$

where x_s is the horizontal orbit offset at the sextupole, and Δk_q the corresponding change in quadrupole gradient. A different approach, tested at KEK [64], is to equip the sextupole magnets with additional quadrupole trim windings for beam-based alignment. This is based on the assumption that the magnetic centers of quadrupole trim coil and sextupole will coincide. Sextupole alignment with a precision better than 50 μm was demonstrated [64].

Local orbit bumps across single sextupoles have been used for the purpose of sextupole alignment at KEK [46,65] and DESY [66]. The strength of all sextupoles is changed together and the induced orbit change is measured. Then the measurement is repeated for a different bump amplitude. The horizontal deflection depends quadratically on the horizontal bump amplitude, while the vertical deflection is a linear function:

$$\Delta\theta_x = -0.5\ K_s(x_{bump} - x_s)^2 \tag{75}$$

$$\Delta\theta_y = K_s(x_{bump} - x_s)y_s \tag{76}$$

where x_{bump} is the amplitude of the bump, and x_s, y_s are the sextupole misalignments. The advantage of this method is that it does not require individual power supplies for the sextupoles.

Alternative approaches are conceivable: one could vary multiple sextupoles at once, and fit for multiple kicks. Also, one could vary the sextupole strength and measure the induced tune variation or the tune separation near the difference resonance [67].

In the final-focus systems of linear colliders, sextupole alignment is essential. At the SLC final focus, the orbit in the sextupoles must frequently be measured and adjusted to maintain a high luminosity. The SLC sextupole alignment is based on varying the sextupole strength and detecting the induced optics (not orbit) change [63]. If the orbit is off center, the first order effect of the sextupole excitation is a waist shift (change in the beta function), skew coupling, or dispersion at the interaction point. These optics changes can be quantified easily by reoptimizing the spot-size at the collision point, after a change in the sextupole strength. The reoptimization is done by scanning a group of quadrupole and skew quadrupole magnets excited together so that they only affect one optical parameter. For each value of the parameter correction, the IP spot size is remeasured with beam-beam deflection scans, and

the magnets are finally set to a value where the beam size is minimum. The change in the optimum waist, dispersion, etc., as a function of the sextupole excitation is proportional to the orbit offset at the sextupole. The measured offsets are corrected by means of closed bumps.

An interesting feature of the SLC final focus is that it has 2 pairs of interleaved sextupoles. The sextupoles in each pair, connected to the same power supply, are separated by an optical $-I$ transform. Thus, the alignment procedure actually consists in generating symmetric or antisymmetric orbit bumps for each sextupole pair, in response to the amount of waist motion or dispersion etc., induced by a change in the sextupole-pair strength[68].

6.4 Sextupole Movement

It is also possible to align the sextupole magnets by detecting the second-order effect of the sextupole excitation: the induced orbit kick. This method works well when the sextupoles are installed on precision movers, which can be used for both the measurement and the alignment. The basic idea is straightforward. Measuring the orbit change downstream as a function of horizontal or vertical sextupole-mover position results in a parabolic curve. The sextupole is aligned when the mover position is set to the minimum of this curve. A sample measurement from the FFTB[69] is displayed in Fig. 23.

6.5 Structure Alignment using Beam-Induced Signals

For future high-gradient linear accelerators it is essential to center the beam orbit in the accelerating structures, thus minimizing the transverse wakefields. Alignment techniques were studied on a test structure for the Next Linear Collider, which was installed in the SLAC linac, as part of the ASSET experiment. These studies demonstrated that the beam-induced dipole-mode signals can be used to center the beam to the level of 40 μm[70]. The result in Fig. 24 shows the amplitude and phase (with respect to a reference phase derived from a BPM signal) of a 15-MHz wide slice of the beam-induced dipole mode signal, centered near 15 GHz, as a function of the nominal beam position. The beam position was varied with dipole steering magnets. Clearly visible is a minimum in the amplitude along with a 180 degree phase jump. Steering the beam to the position with minimum signal successfully centered the orbit in the structure as was verified by detecting the deflection experienced by a subsequent witness bunch.

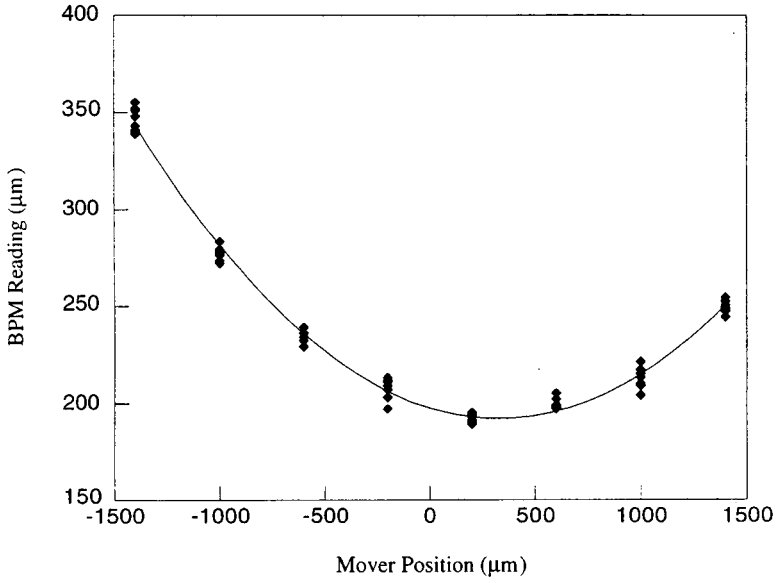

Figure 23: Sextupole alignment in the Final Focus Test Beam (FFTB)[69]: downstream orbit variation is measured as a function of sextupole mover position; the sextupole is aligned at the minimum of the parabola. (Courtesy P. Tenenbaum, 1998.)

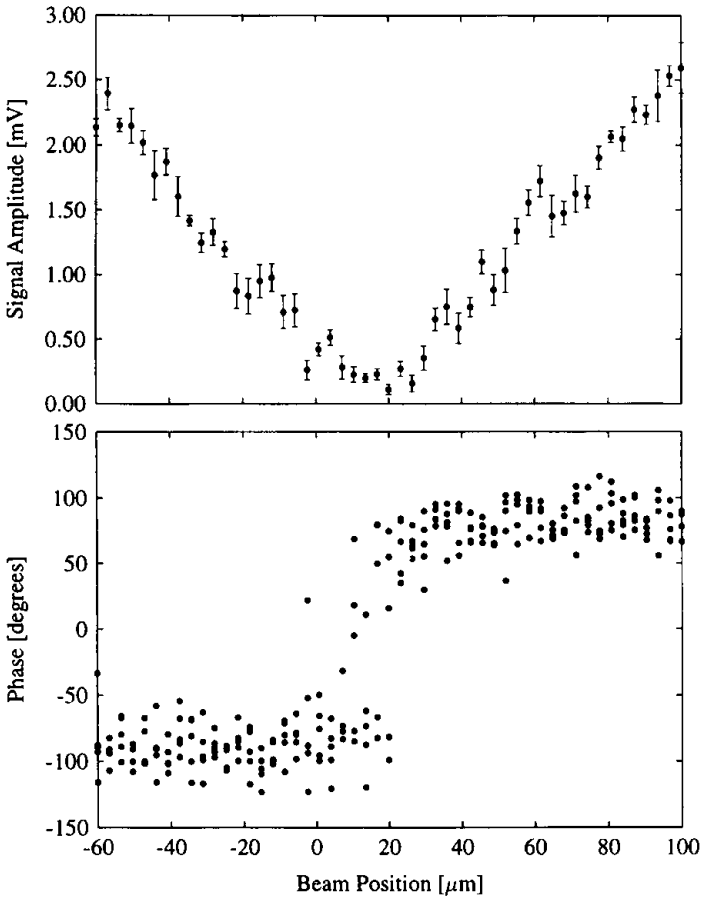

Figure 24: Amplitude (top) and phase (bottom) of the beam-induced dipole mode signal in an X-band accelerating structure versus the nominal beam position (arbitrary zero), which was varied by steering correctors[70]. (Courtesy M. Seidel, 1998).

7 Review of Longitudinal Dynamics

If the energy of the beam, or of a particle in the beam, differs from the design energy its trajectory may deviate from the trajectory of a particle at the right energy. In first order, this deviation is linear in the momentum deviation $\delta = \Delta p/p$. For a transport line we can write

$$\Delta x(s) = R_{16}\delta \tag{77}$$

where R_{16} is the (1,6) transport matrix element from the location where the energy error δ was induced to the location s. In a storage ring, the orbit deviation due to an energy offset is given by the periodic dispersion function $\eta(s)$ as

$$\Delta x(s) = \eta(s)\delta \tag{78}$$

Also the R_{16} matrix element of Eq. (77) is often called dispersion, but it should be kept in mind that this term is not uniquely defined and can be very different for different energy-error sources. As a result, the correction of dispersion in a transport line or a linac can become conceptually quite complicated.

If the beam (or particle) energy is varied, the radius of curvature and, thus, path length in the bending magnet changes. The first order path length change is characterized by the momentum compaction factor α:

$$\alpha = \frac{\Delta L/L}{\delta} = \frac{1}{L}\oint \frac{\eta(s)}{\rho(s)}\, ds. \tag{79}$$

If $\gamma > 1/\sqrt{\alpha}$, a ring is said to operate 'above transition'; this is the case for most electron and high-energy proton rings. For a transport line, α and $\eta(s)$ in Eq. (79) must be replaced by

$$R_{56}(s) = \int_{s_0}^{s} \frac{R_{16}(s')}{\rho(s')}\, ds', \tag{80}$$

where $\mathbf{R}(s)$ is the transport matrix from the location at which the energy is changed (*e.g.*, a cavity) to the location s.

Just as the beam, or an individual particle in the beam, executes betatron oscillations, it also performs oscillations in the longitudinal phase space, in a storage ring with nonzero rf voltage. The frequency of the synchrotron motion is much lower than the two betatron-oscillation frequencies (one synchrotron period typically corresponds to 100s of turns). It can be expressed in terms of a synchrotron tune Q_s (which is the synchrotron frequency f_s in units of the

revolution frequency f_{rev}):

$$Q_s = \frac{f_s}{f_{rev}} = \sqrt{\frac{(\alpha - \gamma^{-2}) h e \hat{V} \cos\psi_s}{2\pi c p_0}} \tag{81}$$

where α is the momentum compaction factor, $\hat{V}$ the amplitude of the rf voltage (assumed as simply sinusoidal), h the rf harmonic number ($f_{rf} = h f_{rev}$), e the particle charge, p_0 the equilibrium momentum, c the speed of light, and ψ_s the synchronous phase angle. The latter is determined by the condition that $e\hat{V}\sin\psi_s = U_0$, where U_0 is the average energy loss per turn.

8 Dispersion

8.1 RF Frequency Shift

In most storage rings the dispersion function is inferred from the orbit change induced by a shift in the rf frequency. A frequency shift Δf_{rf} changes the beam energy by an amount

$$\delta = -\frac{1}{\alpha - \gamma^{-2}} \frac{\Delta f_{rf}}{f_{rf}} \approx -\frac{1}{\alpha}\frac{\Delta f_{rf}}{f_{rf}}. \tag{82}$$

The last approximation, which ignores the change in particle velocity, is applicable for all electron rings. Combining Eqs. (78) and (82), we can relate the dispersion to the measured orbit change:

$$\eta(s) = \left(\gamma^{-2} - \alpha\right) \frac{\Delta x(s)}{\Delta f_{rf}/f_{rf}} \tag{83}$$

This 'static' dispersion measurement is quite simple. It requires the capability of stably unlocking the ring rf frequency (*e.g.*, from the injector rf) and a minimum energy aperture; by energy aperture we here mean the range over which f_{rf} can be changed without beam loss. The residual vertical dispersion is obtained from the vertical orbit shift, in quite the same way.

As an illustration, Fig. 25 shows a static dispersion measurement at the PEP-II HER.

8.2 RF Modulation

In very large rings, operating at high energy, the above method may not be applicable, because of a finite energy aperture and the lack of orbit reproducibility. At LEP, a dynamic measurement is applied [34]: the phase of the rf

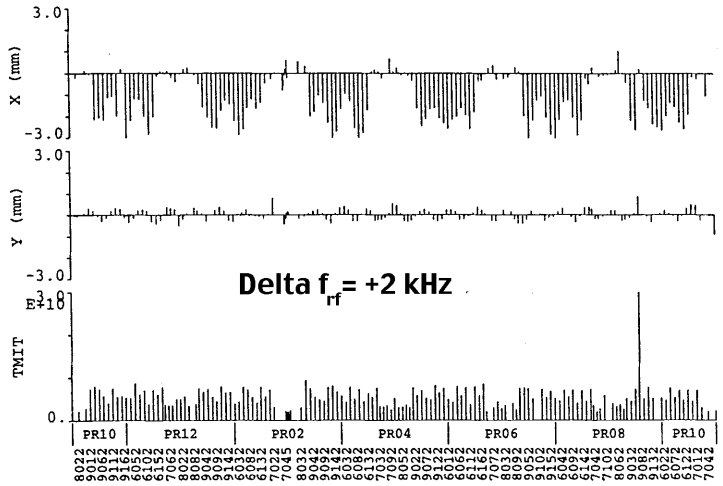

Figure 25: Static dispersion measurement on the PEP-II HER: the orbit change induced by a 2-kHz shift in rf frequency. The nominal rf frequency is 476 MHz; the harmonic number $h = 3492$; and the momentum compaction factor $\alpha \approx 0.0024$. (Courtesy U. Wienands, J. Seeman *et al*, 1998.)

voltage is harmonically modulated at a frequency close to the synchrotron frequency and the frequency component of the induced (resonant) orbit variation at the synchrotron frequency is used to infer the dispersion function at each BPM.

The result of such a dynamic dispersion measurement is displayed in Fig. 26. If the dispersion at the cavities is nonzero, the dynamic measurement will give a result different from the static measurement [71]. The difference has the azimuthal pattern of a betatron oscillation, and it is clearly visible in the figure. At every location s, this component oscillates at the synchrotron frequency, but, in principle, a precise phase measurement from BPM to BPM could be used to correct for this effect.

In the arcs, the maximum value of this spurious dispersion is given by [71]:

$$|\Delta\eta|_{max} = \sqrt{\beta\mathcal{H}_0}\ \left|\frac{\sin(2\pi Q_s)\ \sin(\pi Q)}{\cos(2\pi Q_s) - \cos(2\pi Q)}\right|, \tag{84}$$

where Q and Q_s are the betatron and synchrotron tune, respectively, $\mathcal{H}_0$ is the dispersion invariant [15] in the straight section, and β the arc beta function.

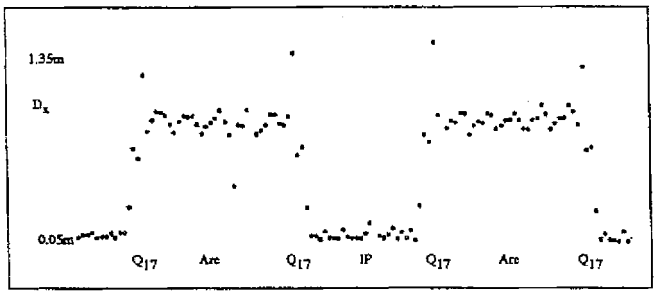

Figure 26: Dynamic dispersion measurement at LEP [34]: the rf voltage is modulated at the synchrotron frequency, and the dispersion deduced by a harmonic analysis of the beam response at each BPM. (Courtesy C. Bovet, 1998.)

8.3 RF Amplitude or Phase Jump

Similar dynamic schemes have been tested at the SLC and at the ATF damping rings. In both these rings, a longitudinal oscillation is induced by a shock excitation: either a sudden step-change to the rf voltage (at the SLC [72]) or a fast phase jump (at the ATF [73]). These methods can also give spurious results if there is residual dispersion at the rf cavities.

On the other hand, the dynamic schemes may be used to correct the synchrobetatron coupling by minimizing the spurious dispersion.

8.4 Higher-Order Dispersion in a Transport Line or Linac

The dispersion (or, more precisely, the R_{16} matrix element) in a transport line can be inferred from the measured variation of the beam orbit as a function of the incoming beam energy. We can extend the concept of dispersion by including higher-order nonlinear terms, of the form:

$$\Delta x(s) = R_{16}(s)\delta + T_{166}(s)\delta^2 + U_{1666}(s)\delta^3 \quad (85)$$

$$\Delta x'(s) = R_{26}(s)\delta + T_{266}(s)\delta^2 + U_{2666}(s)\delta^3 \quad (86)$$

Sufficiently large energy changes allow a measurement not only of the first-order dispersion matrix element, R_{16}, but also of the 2nd and 3rd order contributions, $T_{166}(s)$ and $U_{1666}(s)$.

Such measurements have been performed at the North ring-to-linac transfer line (NRTL) of the SLC. Under normal operation, the phase of the rf compressor at the entrance to the RTL is set so that the beam center passes at the zero crossing of the rf wave. Fpr a dispersion measurement, the phase is

shifted such that the beam center is positioned at the top of the rf crest, and the beam energy is varied by changing the amplitude of the rf voltage.

Figure 27 (top) shows the beam position on one of the RTL BPMs as a function of the beam energy. Clearly visible is a nonlinear dependence, which indicates the presence of 3rd order dispersion. The value of the 3rd order dispersion at this BPM can be obtained by fitting a 3rd order polynomial to the measurement. Plotted in the bottom figure is the 3rd order dispersion function so obtained as a function of position along the RTL and the early part of the SLAC linac.

The large 3rd order dispersion led to undesired and irrecoverable emittance growth. To correct this, in 1991 two octupole magnets were installed which cancel the U_{1666} and U_{2666} terms. The optimum octupole strength was found by minimizing the linac emittance as a function of the octupole excitation. Such a measurement is shown in Fig. 28. The octupole setting for minimum emittance and the corresponding U_{1666} value are in good agreement with the 3rd order dispersion inferred from the BPM readings, which was depicted in Fig. 27 (bottom).

9 Momentum Compaction Factor

It is sometimes of interest to measure the momentum compaction factor α, Eq. (79), for example, in storage rings operating near $\alpha = 0$.

9.1 Synchrotron Tune

If the rf voltage is well calibrated, one can use Eq. (81) to infer the momentum compaction factor from the measured synchrotron tune, taking into account that the synchronous phase angle ψ_s is also a function of the rf voltage. However, often the rf voltage calibration is not very accurate. In addition, if the ring accommodates several rf cavities, these may be not optimally phased with respect to each other, complicating the calculation of the total rf voltage. It is then advantageous to confirm the momentum compaction without having to assume a value for the rf voltage.

9.2 Bunch Length

The rms bunch length in an electron ring is proportional to α and to the rms energy spread [15], namely

$$\sigma_z = \frac{c\alpha}{2\pi Q_s f_{rev}} \sigma_\delta, \tag{87}$$

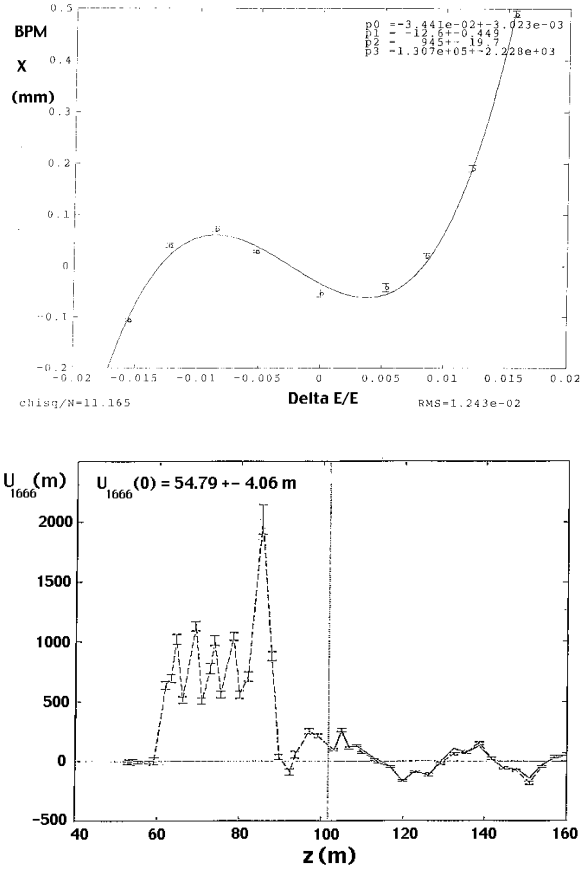

Figure 27: Evidence of 3rd order dispersion in the SLC ring-to-linac transfer line (RTL)[74]: (Top) BPM reading vs. beam energy; (bottom) 3rd order dispersion inferred for all BPMs in the RTL and in the early linac; the 3rd order dispersion in the linac is fitted to calculate the magnitude of the U_{1666} and U_{2666} matrix elements. (Courtesy P. Emma, 1998.)

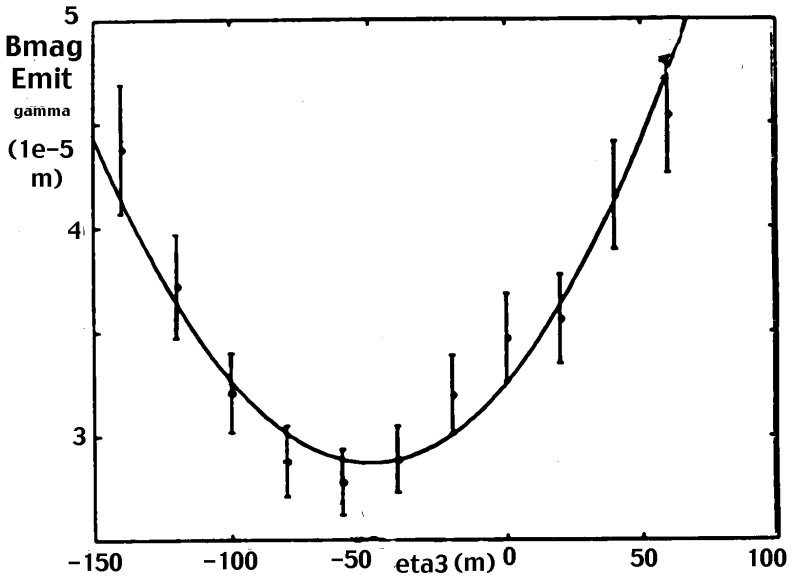

Figure 28: RTL emittance minimization with an octupole correcting the 3rd order dispersion. Shown on the horizontal axis is the octupole strength in units of the generated 3rd order dispersion (U_{1666}). The vertical axis represents the product of Bmag and normalized emittance in units of 10^{-5} m. The octupole strength for which the emittance is minimum agrees with the magnitude of U_{1666} estimated from the fit in Fig. 27 (bottom). (Courtesy P. Emma, 1998.)

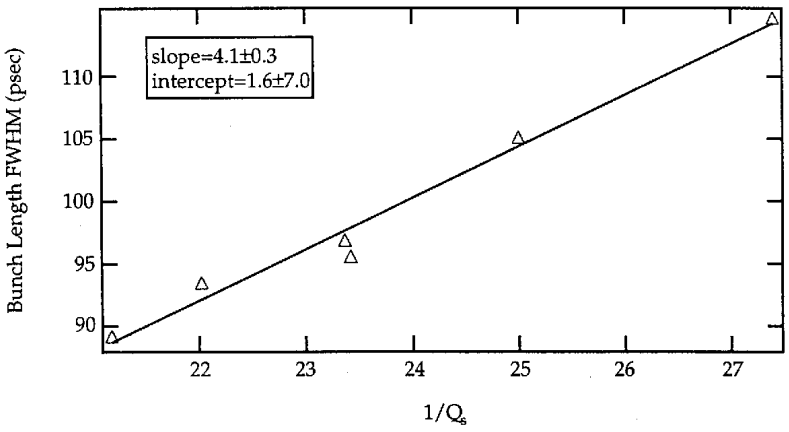

Figure 29: Rms bunch length in the PEP-II HER as a function of the inverse synchrotron tune[77]. The fitted slope determines the momentum compaction factor α, if the rms energy spread is known. (Courtesy U. Wienands, A. Fisher, J. Seeman *et al*, 1998.)

where c is the speed of light, and f_{rev} the revolution frequency. The rms energy spread can either be deduced from the measured decoherence of a transverse oscillation due to nonzero chromaticity and its subsequent recoherence after one synchrotron period[75], or it can be calculated from[15]

$$\sigma_\delta^2 = \frac{C_q < G^3 > \gamma^2}{J_\epsilon < G^2 >} \tag{88}$$

where $C_q = 3.84 \times 10^{-13}$ m, $G = 1/\rho$ the inverse bending radius, $< \ldots >$ indicates an average over the ring, γ is the beam energy in units of the particle rest mass, and J_ϵ the longitudinal damping partition number. The theoretical value for the latter could be verified by measuring either the horizontal emittance (which determines the horizontal partition number $J_x = 3 - J_\epsilon$) or the longitudinal damping time.

Plotting the bunch length as a function of the inverse synchrotron tune immediately gives the value of α as the slope[76]. Note that the synchrotron frequency $f_s = \omega_s/(2\pi)$ can be measured very precisely. Figure 29 shows a measurement of bunch length vs. synchrotron tune in PEP-II.

9.3 Lifetime

A different approach, also applicable for electron rings, is to measure the quantum lifetime [76], which in an electron storage ring is given by [15]

$$\tau_q = \frac{\tau_\delta}{2} \frac{e^\xi}{\xi}, \tag{89}$$

where τ_δ is the longitudinal damping time, and ξ is given by the ratio of the energy aperture δ_{max} and the relative rms energy spread σ_δ:

$$\xi = \frac{\delta_{max}^2}{2\sigma_\delta^2} \tag{90}$$

The energy aperture, if limited by the rf bucket size, is [15]

$$\delta_{max}^2 \approx \frac{eU_0}{\pi\alpha h E_0} F(q) \tag{91}$$

with

$$F(q) = 2\left(\sqrt{q^2-1} - \cos^{-1}(1/q)\right). \tag{92}$$

and

$$q = \frac{e\hat{V}}{U_0} \tag{93}$$

The term $U_0 = C_\gamma E_0^4 L < G^2 > /(2\pi)$, is the energy loss per turn, and $C_\gamma = 8.85 \times 10^{-5}$ m GeV^{-3}. A formula for the rms relative energy spread σ_δ was given in Eq. (88).

We may express σ_δ in terms of σ_z using Eq. (87), and in addition replace the rf voltage $\hat{V}$ in the definition of q by Q_s and α, making use of Eq. (81). We then arrive at an equation for the quantum lifetime τ_q in terms of the measurable quantities Q_s and σ_z, and the unknown parameter α. The latter can then be obtained from a fit to data taken at different rf voltages [76].

9.4 Path Length vs. Energy

The momentum compaction factor, or R_{56} matrix element, can also be measured directly by changing the beam energy at the entrance to the beam line of interest, and observing the shift in arrival time at the end of that section.

Such measurements were performed to fine-tune the optics in the nominally achromatic arc of the KEKB linac. The time of arrival at the exit of the arc was measured by a streak camera. The streak camera converts the time structure of

a pulse of synchrotron radiation from a bend, or of optical transition radiation from a target, into vertical deflection at the CCD camera.

For the KEKB linac commissioning, the streak camera trigger signal was locked to the linac rf frequency upstream of the arc. The beam energy was varied by adjusting the voltage of the last klystrons prior to the arc. Figure 30 shows two measurements of the R_{56}, performed before and after the strengths of a few quadrupoles were adjusted to match the dispersion, as inferred from the energy dependence of the orbit. Figure 30 demonstrates that the dispersion match also eliminated the linear component of the R_{56}. The remaining path length dependence on energy is purely quadratic. In the future, it is planned to reduce this quadratic component, as well as the second order dispersion, by adjusting sextupole magnets.

9.5 Beam Energy via Resonant Depolarization

In electron storage rings with polarization the beam energy can be determined with a very high precision, using a resonant depolarization technique. The spin tune is given by

$$\nu_0 = a_E \gamma = \frac{E\ [\mathrm{MeV}]}{440.6486(1)\ [\mathrm{MeV}]} \tag{94}$$

where a_e is the electron anomalous magnetic moment. If a radially oscillating field generated by a coil is in resonance with the fractional part of the spin tune, the effect of the field adds up over many turns and the spin vector can be brought into the horizontal plane. The exact value of the resonance frequency determines the beam energy via Eq. (94).

With this technique, it is possible to very precisely measure the energy variation induced by a change in the rf frequency. The slope of this measurement gives the momentum compaction factor:

$$\frac{\Delta p}{p} = \frac{1}{\gamma^{-2} - \alpha} \frac{\Delta f_{rf}}{f_{rf}} \approx -\frac{1}{\alpha} \frac{\Delta f_{rf}}{f_{rf}} \tag{95}$$

An application of this technique at LEP is shown in Fig. 31

9.6 Change in Field Strength for Unbunched Proton Beam

The energy of an unbunched proton beam is constant. If the strength of all magnets (dipoles and quadrupoles) is increased by a factor $\Delta B/B$, the orbit moves inwards and the revolution time is reduced. This change in revolution

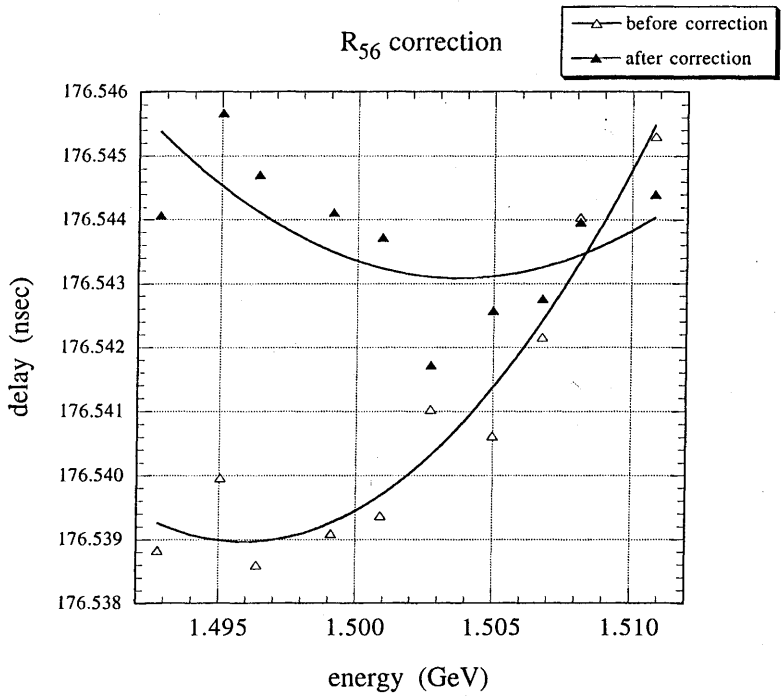

Figure 30: R_{56} measurement for the asynchronous arc of the KEKB linac, before and after dispersion correction, A streak camera was used to measure the arrival time (vertical axis) as a function of the beam energy. (Courtesy H. Koiso and K. Oide, 1998.)

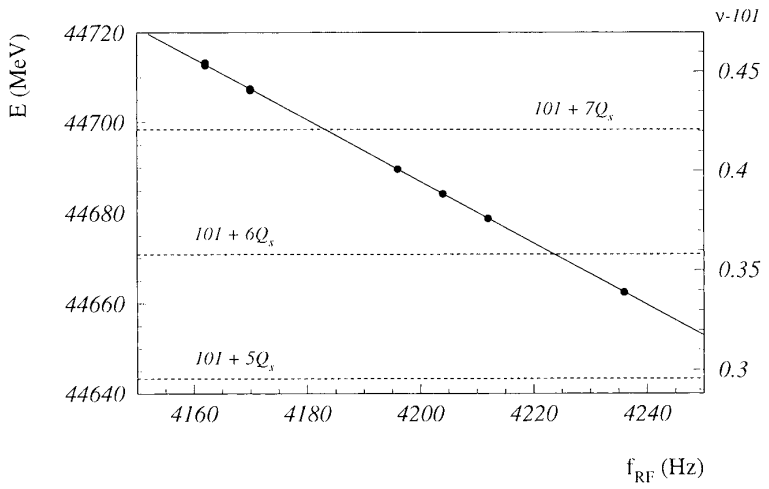

Figure 31: Change of beam energy, E, as a function of the rf frequency, f_{rf}, in LEP[78]. Only the last four digits of the rf frequency are shown (the nominal value is $f_{rf} = 352\ 254\ 170$ Hz). Several strong spin resonances are indicated by the dotted lines. From this measurement the momentum compaction factor was determined to be $(1.86 \pm 0.02) \times 10^{-4}$, which compared well with the calculated value of 1.859×10^{-4}. (Courtesy R. Assmann, 1998).

period can be detected with a Schottky monitor[79]. The momentum compaction factor α then simply follows from the relation

$$\frac{\Delta T}{T} = -\alpha \frac{\Delta B}{B} \tag{96}$$

where T denotes the revolution period.

10 Chromaticity

10.1 RF Frequency Shift

The dependence of the focusing force on beam energy is generically referred to as chromaticity. In a storage ring this is characterized by the energy dependence of the betatron tunes, which is denoted as ξ.

The natural chromaticity due to the energy dependence of the quadrupole focusing is usually compensated by means of two or more sextupole families. Usually a total chromaticity close to zero is desired, as this minimizes the tune spread induced by chromaticity and finite energy spread, and also the amount of synchrobetatron coupling. The chromaticity should be slightly positive to avoid the head-tail instability. Since a positive chromaticity gives head-tail damping, sometimes ξ is intentionally increased in order to counteract beam instabilities.

The total chromaticity can easily be determined by measuring the tune shift as a function of the rf frequency f_{rf}.:

$$\xi_{x,y} = \frac{\Delta Q_{x,y}}{\Delta p/p} = \left(\gamma^{-2} - \alpha\right) \frac{\Delta Q_{x,y}}{\Delta f_{rf}/f_{rf}} \tag{97}$$

where α is the momentum compaction factor. As an example, Fig. 32 shows a chromaticity measurement performed at LEP.

10.2 Head-Tail Phase Shift

Recently, a new technique to measure the chromaticity was successfully tested at the CERN SPS [25]. A bunch was kicked transversely, and the linear head-tail phase shift $\Delta\phi_\beta$ as a function of arrival time Δt was measured half a synchrotron period later. The chromaticity is then obtained from the relation

$$\xi = -\frac{\omega_s \left(\alpha - \gamma^{-2}\right)}{2\omega_0} \frac{\Delta\phi_\beta}{\Delta t} \tag{98}$$

The advantage of this method is that it is very fast.

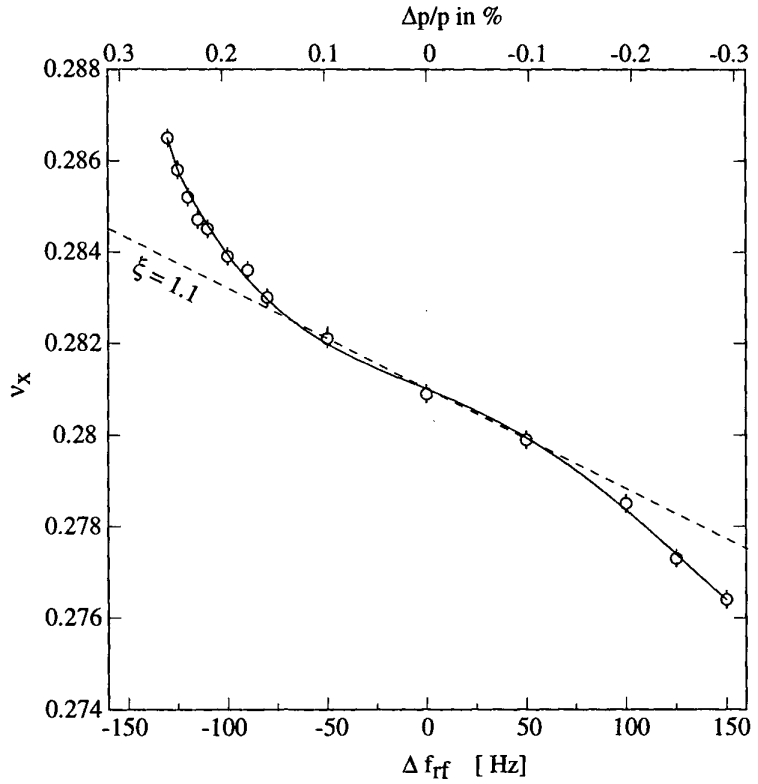

Figure 32: Horizontal tune as a function of the rf frequency change in LEP. Plotting symbols with error bars are the data. The dashed line is the linear chromaticity as calculated from tune measurements at $\Delta f_{rf} = \pm 50$ kHz. (Courtesy H. Burkhardt, 1998.)

10.3 Natural Chromaticity

The natural chromaticity is the chromaticity that derives from the energy dependence of the quadrupole focusing. In other words it is the chromaticity the ring would have without sextupole magnets. Fortunately it is not necessary to turn off the sextupoles to measure the natural chromaticity. Rather the latter can be obtained by detecting the variation of the betatron tune as a function of the main dipole field strength. In this case, since the rf frequency and, hence, the total path length are unchanged, the orbit in the sextupoles remains approximately the same, and the sextupoles thus do not contribute to any tune change. (This is a good assumption for FODO lattices. However, it is conceivable that for certain low-emittance lattices, the orbit in the sextupoles might change when the dipole field strength is varied. This effect can be estimated with computer codes. One can also monitor the orbit stability at the sextupoles when the dipole field is varied.) However, the absolute beam energy E is changed in proportion to the field change: $\Delta E/E = \Delta B/B$. Thus, the natural chromaticity $\xi_{x,y}^{nat}$ is given by

$$\xi_{x,y}^{nat} \approx \frac{\Delta Q_{x,y}}{\Delta B/B} \tag{99}$$

A typical measurement is depicted in Fig. 33.

10.4 Local Chromaticity: $d\beta/d\delta$

Measuring the beta functions (*e.g.*, with the tune shift method of Eq. (32)) for different values of the rf frequency yields informations on the local chromaticity. This can help to identify the origin of chromatic errors or to find sources of chromatic nonlinearities.

10.5 Chromaticity Control in Superconducting Proton Rings

In superconducting proton rings the natural chromaticity is small compared with the chromaticity arising from the persistent-current sextupole components in the dipole magnets. For example, in the HERA proton ring the sextupole component in the dipoles contributes a chromaticity that is 5 times larger than the natural chromaticity. At injection energy, a significant part of the persistent current decays in time, causing a large variation in chromaticity. This is illustrated in Fig. 34, which also demonstrates the effect of an automatic correction system. The correction is done locally, by exciting sextupole correction coils mounted inside all bending magnets. The excitation for these correction

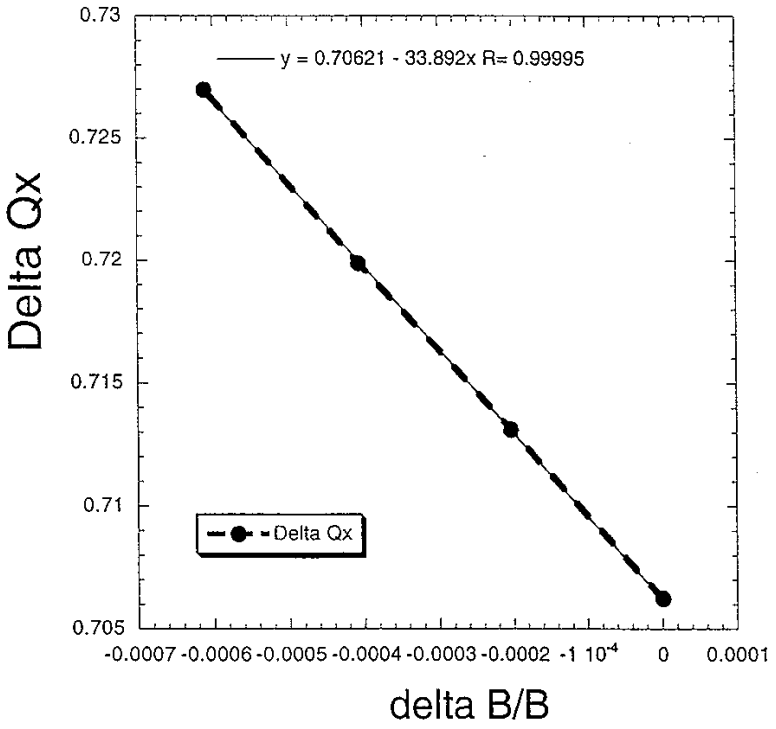

Figure 33: Measurement of the natural chromaticity in the PEP-II HER. Shown is the horizontal tune as a function of a relative variation in the main dipole field. The slope is the natural chromaticity. (Courtesy U. Wienands, J. Seeman *et al*, 1998.)

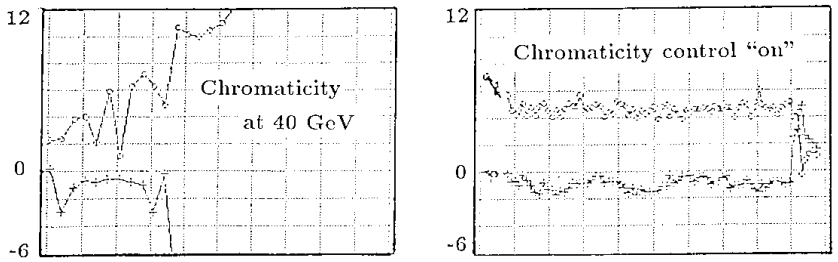

Figure 34: Variation of chromaticity in time, due to persistent-current decay without (left) and with (right) chromaticity control based on continuous measurements of the sextupole fields in two dipole reference magnets at the HERA proton ring. The horizontal axis is the time in units of 3 minutes per division. The vertical axis refers to the horizontal (upper trace) and vertical chromaticity (lower trace) in dimensionless units. (Courtesy B. Holzer, 1998.)

magnets is determined from the instantaneous sextupole field measured by rotating coils in two reference magnets, which are connected in series with the main superconducting magnet circuit.

The persistent-current sextupole field in the dipole magnets decays during injection at 40 GeV. It is reinduced at the start of acceleration, resulting in large variations of the chromaticity. Figure 35 shows the change in chromaticity during acceleration from 40 GeV to 70 GeV. The figure compares the actual chromaticity, *i.e.*, the change in tune detected per relative rf frequency change, Eq. (97) [80], measured without continuous correction; the chromaticity predicted by the reference magnets; and the chromaticity measured with a correction derived from the reference magnets.

Another noteworthy feature of the persistent-current sextupole field is that it is not very reproducible from cycle to cycle. An example of the nonreproducibility is depicted in Fig. 36. After each magnet cycle, when the ring is back at injection energy, the chromaticity is first corrected by means of a direct measurement (tune shift versus rf frequency). Subsequently, the chormaticity is held constant using the automatic control based on the reference magnets.

10.6 Application: Measuring the Central Frequency

Measuring the chromaticity for different sextupole strengths determines the 'central frequency'. This is the rf frequency for which the orbit on average passes through the center of all sextupoles [81,82]. An example of such a mea-

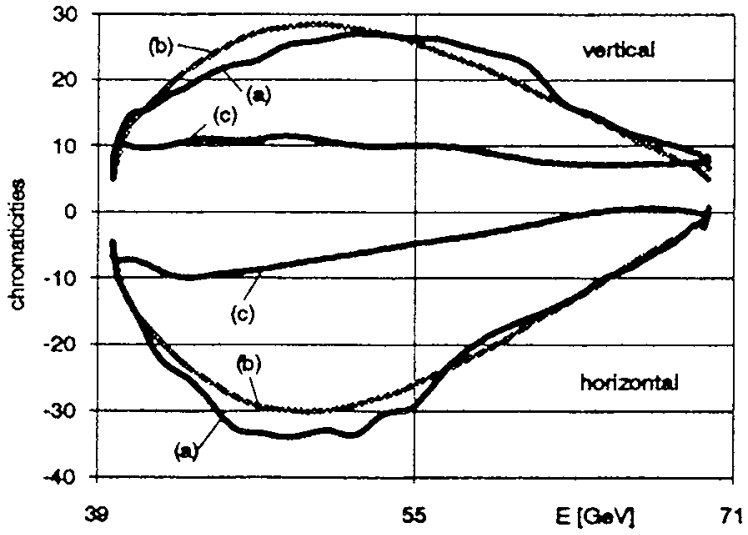

Figure 35: Variation of the chromaticity in the HERA proton ring during acceleration from 40 GeV to 70 GeV[80]: (a) measured chromaticity without correction; (b) change in chromaticity derived from the reference-magnet measurements; (c) measured chromaticity with correction. (Courtesy O. Meincke, 1998.)

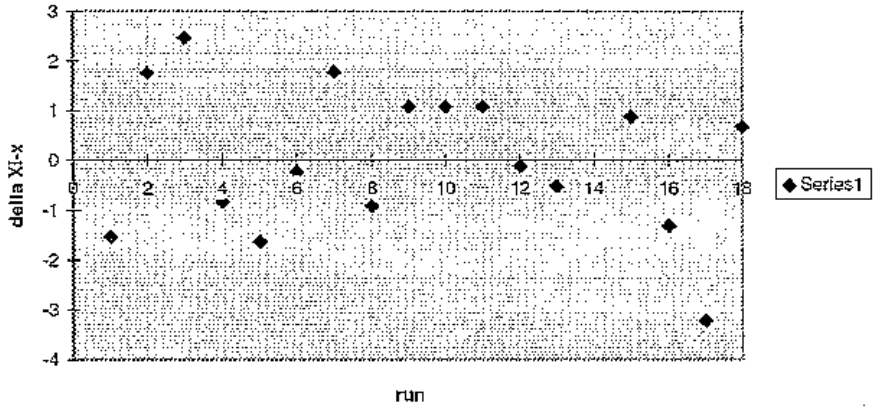

Figure 36: (Ir)reproducibility of the chromaticity for different machine cycles of the HERA proton ring. (Courtesy B. Holzer, 1998.)

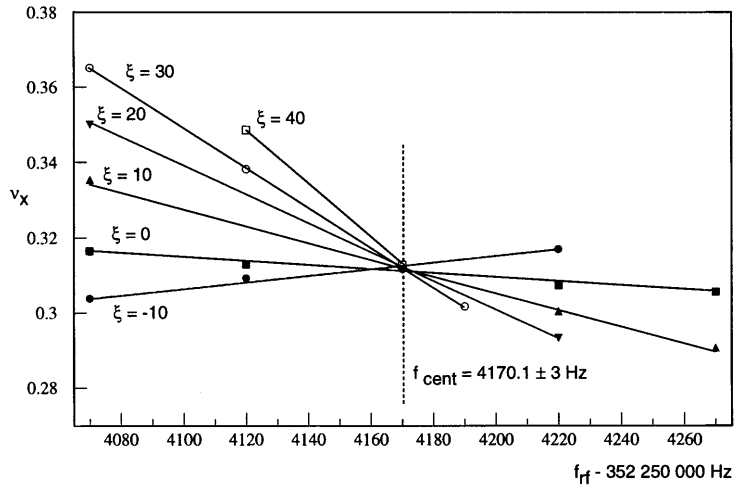

Figure 37: LEP chromaticity measurements for different sextupole excitation patterns, with net chromaciticities in the range $\xi = -10$ to $+40$. The intersection of the different lines determines the central frequency, where the orbit is on average centered in the sextupoles. (Courtesy H. Burkhardt, 1998.)

surement is shown in Fig. 37. Usually adjacent sextupoles and quadrupoles are well aligned with respect to each other, so that one can expect that at the central frequency the beam also passes (on average) through the center of the quadrupoles.

On close view, four different center frequencies can be measured by changing the strength of the horizontal or vertical sextupole families and by measuring the resulting change in the horizontal or vertical tune, respectively. In most cases, the four central frequencies so obtained are found to be the same, supporting the hypothesis that the magnets are usually well aligned on short length scales.

This method allows one to monitor changes of the beam energy, using the relation

$$\frac{\Delta p}{p} = \left(\frac{1}{\gamma^{-2} - \alpha}\right) \frac{\Delta f_{rf}}{f_{rf}} \tag{100}$$

and the fact that the quadrupoles and sextupoles are well aligned with respect to each other. This energy-monitoring technique was applied at BEPC[83] and LEP[84].

11 Coupling

Skew quadrupole field errors and detector solenoids generate betatron coupling between the horizontal and vertical plane of motion. Spurious betatron coupling is a concern, since it may reduce the dynamic aperture [85], and since, in electron machines, it contributes to the vertical equilibrium emittance. The coupling of horizontal and vertical oscillations generates two new eigenmodes of oscillation. These eigenmodes are no longer purely vertical or purely horizontal, but rather they correspond to oscillations whose reference planes are tilted and rotate with the azimuthal position s. In this case, new coupled beta functions can be defined [87,88,89,86].

The important coupling parameters are the two driving terms for the sum and difference resonances, which are given by [86,85,90]:

$$|\kappa_\pm| = \frac{1}{2\pi} \oint ds\ K_s(s) \sqrt{\beta_x(s)\beta_y(s)}\ e^{i(\phi_x \pm \phi_y - (Q_x \pm Q_y - q_\pm) 2\pi s/L)} \tag{101}$$

where K_s is the normalized gradient of the skew quadrupole (in units of m^{-2}), L is the circumference, $\beta_{x,y}$ are the uncoupled beta functions, and we assume that the betatron tunes are near the resonance:

$$Q_x \pm Q_y + q_\pm = 0 \tag{102}$$

where $q_\pm$ is an integer. The dynamic aperture or the beam lifetime of colliding beams can be increased by measuring and minimizing the two driving terms $|\kappa_\pm|$.

In an electron storage ring, the vertical emittance contribution due to weak betatron coupling is [91]

$$\gamma\epsilon_y = \frac{C_q \gamma^3}{16 \oint G^2 ds} \oint \mathcal{H}_x |G^3| \left[\sum_\pm \frac{|W_\pm(s)|^2}{\sin^2 \pi(\Delta Q_\pm)} + \frac{2\mathrm{Re}\left\{W_+^*(s) W_-(s)\right\}}{\sin \pi(\Delta Q_+) + \sin \pi(\Delta Q_-)} \right] ds \tag{103}$$

where $C_q = 3.84 \times 10^{-13}$ m, $\mathcal{H}_x$ is the horizontal dispersion invariant, $G = 1/\rho$ the inverse bending radius, $*$ is the complex conjugate, Re gives the real portion of its argument, $\Delta Q_\pm = Q_x + Q_y \pm q_\pm$, and

$$W_\pm(s) = \int_s^{s+L} dz\ K(z) \sqrt{\beta_x \beta_y} e^{i[(\phi_x(s) \pm \phi_y(s)) - (\phi_x(z) \pm \phi_y(z)) + \pi(Q_x \pm Q_y)]} \tag{104}$$

are the driving terms, including all Fourier components. Note that $|W_{\pm}(0)| = |\kappa_{\pm}|$.

Equation (103) shows that, in order to minimize the vertical emittance, the driving terms $W_{\pm}(s)$, for the two nearest sum and difference resonances, should be corrected.

11.1 First Turn Analysis

Large coupling sources can be identified as locations where a horizontal orbit change generates a vertical kick and vice versa. In order to find such locations, the orbit is changed in one plane, by exciting steering correctors or by changing injection conditions (kicker amplitude), and the effect on the orbit in the perpendicular plane is measured. The same type of analysis can be applied to a transport line.

Large numbers of orbits and BPM data for excitations of different correctors can be fitted to determine the skew quadrupole component of each magnet in the beam line.

11.2 Beam Response after Kick

The driving term $|\kappa_-|$ may be measured by first kicking the beam, and then observing its response in the plane of the kick over *many turns*.

In the vicinity of the difference resonance, the envelopes of the oscillations in the horizontal and vertical plane exhibit a beating (energy exchange between the two planes) with a characteristic total modulation amplitude of [92,86]

$$S = \frac{\hat{x}^2_{min}}{\hat{x}^2_{max}}. \tag{105}$$

Here $\hat{x}$ denotes the envelope of the betatron oscillation in the plane in which the kick was applied; $\hat{x}_{min}$ is its minimum value, and $\hat{x}_{max}$ its maximum value; these two extreme values are assumed alternately, with a modulation (or beating) period T. The driving term for the difference resonance, $|\kappa_-|$ of Eq. (101), is given by [92]

$$|\kappa_-| = \frac{\sqrt{1-S}}{f_{rev}T} \tag{106}$$

Thus a measurement of the modulation period T and the squared envelope ratio S after a kick is sufficient to infer $|\kappa_-|$.

An example from the ATF Damping Ring is shown in Fig. 38. The frequency spectrum from a horizontal BPM signal is viewed over a wide frequency range on a spectrum analyzer (left figure), and the frequency of the betatron

signal is identified as the peak of the spectrum. The span of the spectrum analyzer is then set to zero, and its center set to the betatron frequency. This produces a signal proportional to the square of the betatron-oscillation amplitude. The output signal of the spectrum analyzer can be viewed on an oscilloscope, with results as displayed in Fig. 38 (right). The slow oscillation in this picture corresponds to synchrotron motion (the BPM is at a dispersive location), while the fast beating reflects the transverse coupling. The picture was taken for a tune separation of $|Q_x - Q_y + q_-| \approx 0.02$. If the two tunes are separated further, the modulation period increases and the modulation amplitude decreases. Using Eq. (106) with $T \approx 17.6$ μs and $S \approx 0.3$-0.7, we infer a coupling term of $|\kappa_-| \approx 0.02$, consistent with other measurements[93].

It is of course possible to perform a much more detailed analysis of multiturn BPM data. For example, one can determine the evolution of the coupled optical functions (*e.g.*, the tilt angle of the two transverse eigenplanes) around the ring. An example may be found in Ref.[94].

11.3 Closest Tune Approach

Near the difference resonance, the tunes of the two coupled eigenmodes in the vertical plane are[86,92]

$$Q_{I,II} = \frac{1}{2}\left(Q_x + Q_y + q \pm \sqrt{(Q_x - Q_y + q)^2 + |\kappa_-|^2}\right) \qquad (107)$$

where Q_x and Q_y are the tunes which one would expect without coupling. A similar formula, with the same fractional values of $Q_{I,II}$, describes the coupled tunes in the horizontal plane. Equation (107) shows that the measured tunes, Q_I and Q_{II}, are never exactly equal, but can only approach each other up to a distance $|\kappa_-|$. Figure 39 illustrates this with an example from the PEP-II HER. A common technique for correcting the betatron coupling in a storage ring is to minimize the distance of closest approach using at least two skew quadrupole magnets. It is often the only correction necessary, especially if the tunes are close to the difference resonance $Q_x - Q_y + q = 0$ (q integer).

11.4 Compensating the Sum Resonance

In the vicinity of the difference resonance, there is a continuous energy exchange between the two transverse planes, but the beam or particle motion remains bounded. By contrast, close to the sum resonance, for $|Q_x + Q_y + q| < |\kappa_+|$, the motion is unstable. The total width of the stop band around the sum resonance is equal to the driving term $|\kappa_+|$ of Eq. (101)[86]. Although this may

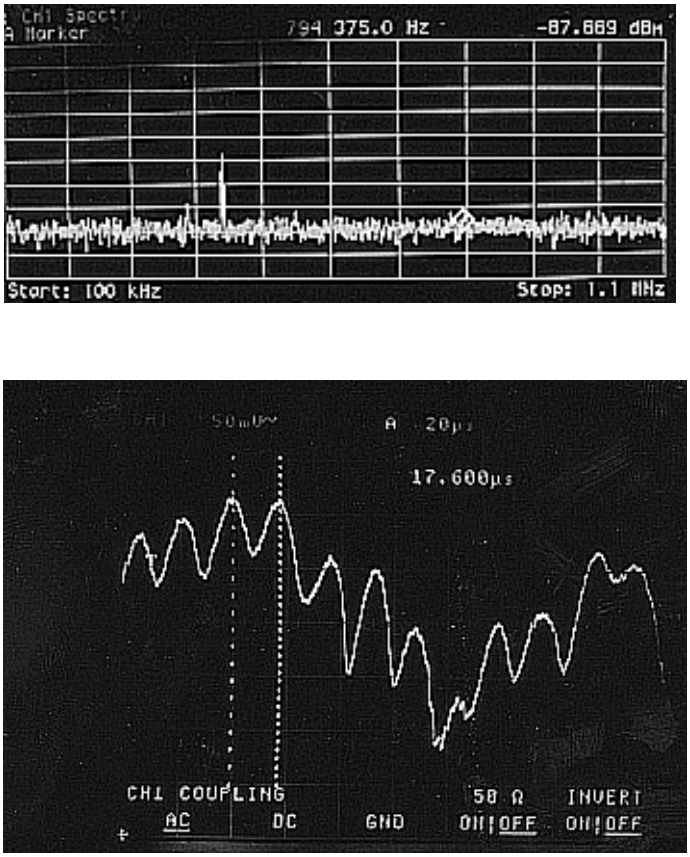

Figure 38: Monitoring betatron coupling at the ATF Damping Ring [93]. (Top) frequency spectrum of a horizontal pick up on a spectrum analyzer; (bottom) evolution of the peak signal in the frequency spectrum as a function of time, as viewed on an oscilloscope; the slow variation reflects synchrotron motion, the fast beating with a period of about 17.6 μs is due to the transverse coupling; the amplitude and period of the modulation can be used to determine the driving term $|\kappa_-|$. (Courtesy M. Minty, 1998.)

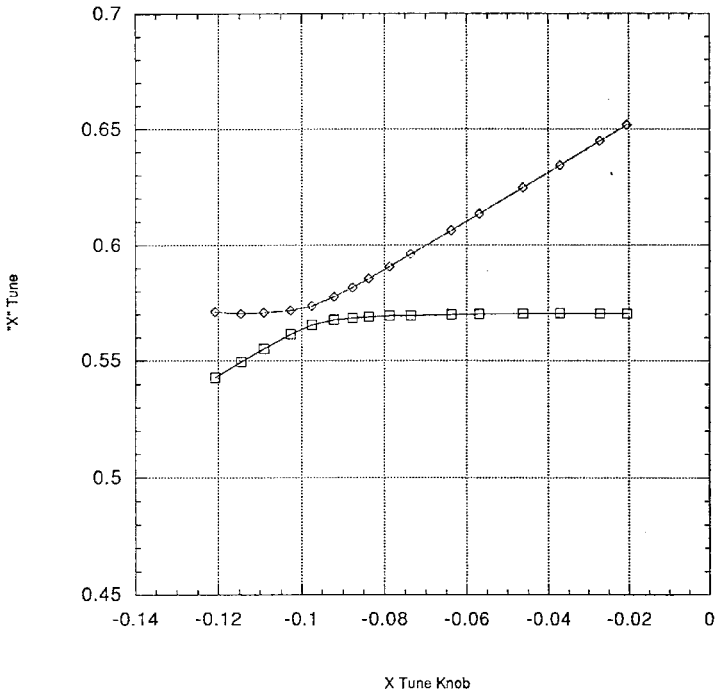

Figure 39: Closest tune approach in the PEP-II HER before final correction[95]. Shown are the measured tunes as a function of the horizontal tune 'knob' (which would only change Q_x if the machine were uncoupled), in dimensionless units. The minimum tune distance is equal to the driving term $|\kappa_-|$ of the difference resonance. (Courtesy Y. Cai, 1998.)

be more difficult in practice than to determine the driving term $|\kappa_-|$ for the difference resonance, from the closest-tune approach, the driving term $|\kappa_+|$ can be compensated by adjusting two skew quadrupoles so as to minimize the stop band width of the sum resonance.

Equation (103) shows that in order to optimize the vertical emittance in a damping ring, in general it is necessary to correct both driving terms, $|\kappa_-|$ and $|\kappa_+|$. The minimum number of skew quadrupole correctors needed to correct both coupling driving terms as well as the vertical dispersion function is six (one sine-like and one cosine-like corrector are required for each effect).

11.5 Coupling Transfer Function

A different method of measuring the coupling is through the 'coupling transfer function' [96]. Here, the beam is excited horizontally, while detecting the resulting vertical coherent motion. Such a technique was used to continually monitor and correct the coupling strength during collisions in the CERN ISR [96].

12 Orbit

12.1 Orbit Correction

If the orbit is off-center in a quadrupole magnet, dispersion is generated, and, in a ring, also the beam energy may be changed or the depolarization may increase. An orbit that is off-center in a sextupole induces skew coupling and/or beta beating. Thus it is very important to center the orbit in these magnets. The standard tools for correcting the orbit are steering corrector magnets. Of course, such an orbit correction will never be perfect. Figure 40 shows a typical absolute orbit reading from the PEP-II HER, after moderate orbit correction during commissioning.

However, there are complications to the above simple idea. If the electronic (or mechanical) offset of the BPM with respect to an adjacent quadrupole has been determined by beam-based alignment and then removed (in the read-out software), orbit correction amounts to minimizing the BPM orbit readings. However, if the BPM offsets are not known, and possibly larger than the alignment errors, a better strategy is to reduce the rms strength of the steering correctors, and to pay less attention to the absolute orbit reading. In several cases, at the SLC and at the ATF, this second approach significantly reduced the magnitude of the residual vertical dispersion [97]. Sometimes other constraints are imposed on the orbit. For example, a certain orbit amplitude or a certain angle may be desired near the injection or extraction points, or near a

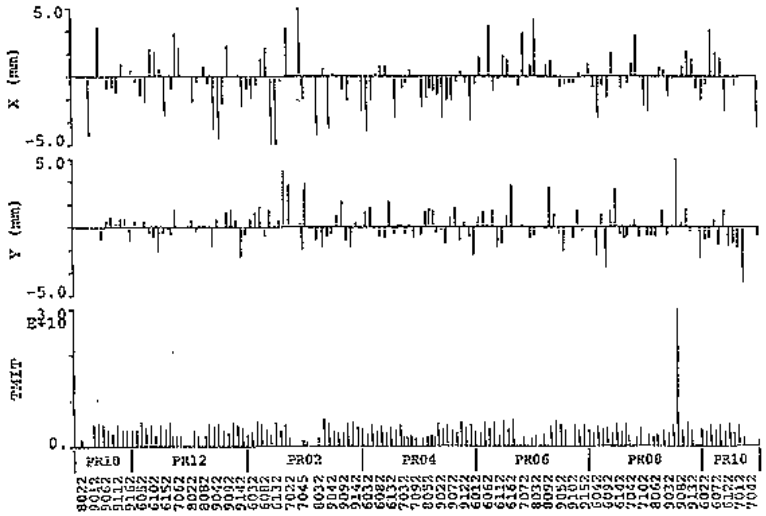

Figure 40: Typical commissioning orbit in the PEP-II HER: (top) horizontal orbit in mm; (center) vertical orbit in mm; (bottom) intensity in 10^{10}. (Courtesy U. Wienands, J. Seeman *et al*, 1998.)

synchrotron light beamline. In such cases, a constant orbit must be maintained at the adjacent BPMs.

12.2 Singular Value Decomposition

A common situation is that the BPM offsets are known fairly well and the orbit already fulfills a number of constraints, but many of the corrector magnets are strongly excited with some of them 'fighting' (compensating) each other. Fortunately, there exists a very powerful technique to reduce the rms strength of the orbit correctors, while maintaining a set of constraints. This technique is sometimes called 'corrector ironing'[98] and it is based on a 'singular value decomposition'[99].

Suppose we want to solve the linear equation

$$\mathbf{\Delta x} = \mathbf{A} \cdot \theta \tag{108}$$

where the vector $\mathbf{\Delta x} = (\Delta x_1, \ldots \Delta x_M)$ may describe the desired correction (or constraint) at M BPMs, and $\theta = (\theta_1, \ldots, \theta_N)$ are the excitation strengths of N correctors, that we want to determine. If $M \geq N$, we can decompose the

matrix $\mathbf{A}$ as

$$\mathbf{A} = \mathbf{U} \cdot \begin{pmatrix} w_1 & 0 & \dots & 0 \\ 0 & w_2 & \dots & 0 \\ & \dots & \dots & \\ 0 & 0 & \dots & w_N \end{pmatrix} \cdot \mathbf{V}^t \tag{109}$$

The column vectors of the $M \times N$ matrix $\mathbf{U}$ and the $N \times N$ matrix $\mathbf{V}$ are orthonormal

$$\mathbf{U}^t \cdot \mathbf{U} = \mathbf{I}_N \tag{110}$$

$$\mathbf{V}^t \cdot \mathbf{V} = \mathbf{I}_N \tag{111}$$

where $\mathbf{I}_N$ denotes the $N \times N$ unity matrix. The decomposition of Eq. (109) can be performed, for example, using the FORTRAN subroutine described in Ref.[99]. An SVD decomposition is also provided in a convenient form by many mathematical analysis packages, such as MATLAB[100].

We now consider three different cases: First, we suppose the number of correctors is equal to the number of BPMs. In this case the matrix $\mathbf{A}$ is square. We can write down a formal solution

$$\theta = \mathbf{A}^{-1} \cdot \mathbf{\Delta x} = \mathbf{V} \cdot \begin{pmatrix} 1/w_1 & 0 & \dots & 0 \\ 0 & 1/w_2 & \dots & 0 \\ & \dots & \dots & \\ 0 & 0 & \dots & 1/w_N \end{pmatrix} \cdot \mathbf{U}^t \cdot \mathbf{\Delta x} \tag{112}$$

If none of the w_i is zero, this is the unique solution to the problem. If one or more of the w_i are zero, the equation may not have an exact solution, but for these w_i one can simply replace $1/w_i$ by 0, and with this replacement Eq. (112) still gives the solution in a least squares sense. This means it minimizes the distance $r = |\mathbf{A} \cdot \theta - \mathbf{\Delta x}|$. Furthermore, the solution vector θ so obtained is the (either least-squares or exact) solution with the smallest possible length $|\theta|^2$. In other words, the solution derived from the SVD decomposition also minimizes the rms strength of the correctors.

In addition, it is worthwhile to note that the columns of $\mathbf{U}$ whose same numbered w_i are nonzero are an orthonormal set of basis vectors that span the range of the matrix $\mathbf{A}$ while the columns of $\mathbf{V}$ whose same-numbered elements w_j are zero are an orthonormal set for the nullspace of $\mathbf{A}$.

Next, we consider the case that there are fewer equations than correctors. In this case, we can simply add rows with zeroes to the vectors and matrices of Eq. (109) until the matrix is square, and then apply the SVD formalism, as described above. In this case, there is (at least) one zero eigenvalue w_j for every row of zeroes added.

Finally, in the case of more BPM constraints than unknown correctors ($M > N$), SVD works just as well. In general the w_j will not be zero, and the SVD solution will agree with the result of a least-square fit. If there are still some small values w_j, these indicate a degeneracy in $\mathbf{A}$ and the corresponding $1/w_j$ should be set to zero, as before. The corresponding column in $\mathbf{V}$ deserves attention, since it describes a linear combination of corrector excitations, which does not affect the constraints.

The SVD steering algorithm has been used successfully at many accelerators, for example, at the synchrotron light source SPEAR [101] or throughout the SLC.

12.3 Orbit Feedback

Feedback systems that stabilize the beam orbit are becoming more common in accelerators, both in light sources, such as the APS, and in accelerators for high-energy physics, such as the SLC [102]. A comprehensive overview of orbit feedback systems can be found in Ref. [103]. A simple orbit feedback maintains a constant orbit by adjusting the strength of 2 or 4 steering correctors based on BPM readings. Many orbit feedback systems employ an SVD algorithm which flattens the orbit while at the same time minimizing the strength of the correctors.

Slightly more complicated feedback loops are designed so that they maintain both the beam orbit and the beam energy. Orbit and energy can be separated using BPMs at dispersive locations. The orbit is corrected via steering correctors; the beam energy by adjustments to some upstream rf phase.

The effectiveness of a feedback can be tested by measuring its response to a step change. An example in Fig. 41 shows the response of an SLC feedback loop to a sudden step change in energy. The picture illustrates the improvement achieved by increasing the number of feedback BPMs.

There are different techniques to calibrate the local transport matrices between correctors and BPMs within each feedback loop, which are used to continually compute the excitation of the feedback steering correctors. For example, the induced change in orbit position and angle can be measured as a function of the individual feedback corrector strengths.

If there are successive feedback loops on a beam line, these loops could interfere with each other, and *e.g.*, cause unwanted orbit oscillations. This interference can be avoided by either one of 4 different approaches [103]: (1) orthogonality, (2) different speed, (3) inter-loop communication (feedback cascades) and (4) integration into one global loop. At the SLC, the orbit feedbacks in the linac are connected by an adaptive cascade. Each feedback passes its

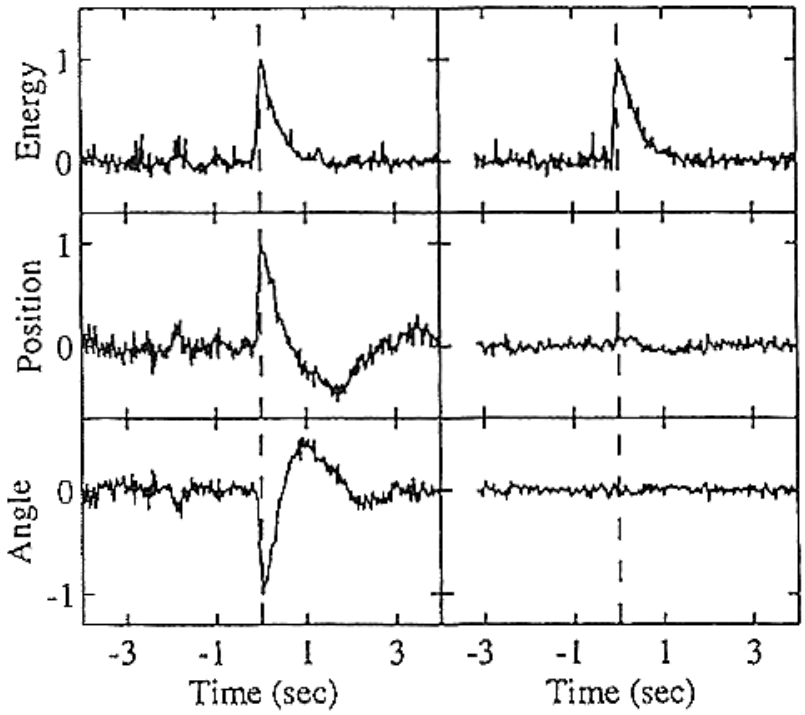

Figure 41: Response of the orbit and energy feedback in the ring-to-linac transfer line of the SLC to a fast step change in energy[102]: (left) before and (right) after additional BPMs were included in the feedback loop. (Courtesy M. Minty, 1998.)

information to the loop downstream, in order to avoid overcorrection of the same perturbation. The linear transport matrix between successive loops is measured continuously using natural beam orbit jitter.

13 Optics Monitoring, Tuning and Feedback

13.1 Tune, Chromaticity and Coupling Control

The simplest control of linear optics in a storage ring is the control of the betatron tune. Phase locked loops (PLL) can be used to track the tune history; see Section 3.4. If a correction is desired, current can be fed to (at least) two quadrupole strings so as to keep the PLL tune signal at a constant value. As mentioned in Section 11.5, at the ISR a crossplane coupling transfer function was measured to monitor and control the betatron coupling with colliding beams. In principle, the dispersion and chromaticity in a storage ring could also be continually controlled using automatic correction loops, which correlate tune signal and orbit to small rf frequency changes, and vary some quadrupole or sextupole correctors to feedback on these signals. An on-line chromaticity measurement is available at HERA, but its result is not used as input for a chromaticity feedback. It appears that most present-day storage rings have no need for elaborate dispersion or chromaticity feedback systems.

For linear colliders, however, similar corrections are essential to achieve the desired luminosity. At the collision point of the Stanford Linear Collider (SLC), dispersion, coupling, and waist positions must be corrected every few minutes [104]. In previous years, this correction was based on beam-beam deflection scans [105], which infer the convoluted interaction-point spot size from the deflection angle as a function of the beam-beam offset [106]. These deflection scans were performed for several different values of orthogonal magnet combinations, or multiknobs (see Section 13.3). Different multiknobs were scanned one by one, and set to the value where the beam size was minimum. Typically, the beam size was measured for 5 different knob settings, and the minimum was determined by a parabolic fit. Examples for all 10 IP aberration scans are shown in Fig. 42.

Nowadays, the SLC luminosity optimization is performed by a fully automatic feedback system, which measures the response of a luminosity-related signal (beamstrahlung) to small changes in the multiknobs [105].

In addition to optics corrections based on beam signals, there are also indirect possibilities to correct and control the optics. For example, in Section 10, we described how the chromaticity in the HERA proton ring is continually corrected with the help of reference magnets.

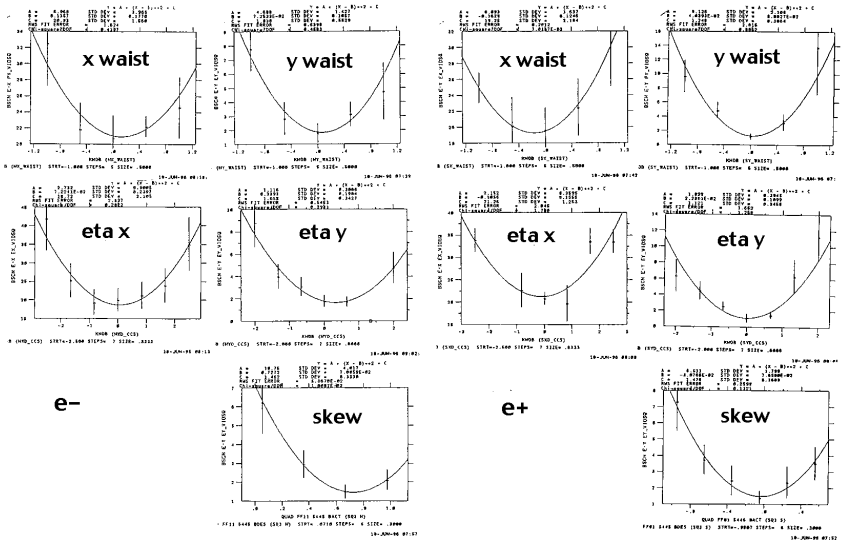

Figure 42: Aberration scans at the SLC collision point. The pictures show the square of the horizontal or vertical beam size measured as a function of different multiknobs. In total, 10 aberrations must be controlled: horizontal and vertical dispersion and waist position, as well as coupling from the horizontal into the vertical plane, for either beam. These aberrations are corrected using different combinations of quadrupole and skew quadrupole magnets which form orthogonal multiknobs. Each multiknob is adjusted so as to minimize the IP spot size, based on a parabolic fit to the beam sizes measured for different knob values. Until 1997 the beam size was inferred from beam-beam deflection scans, with results as shown in the figure. The errors were significant [104]. Nowadays, the aberrations are controlled by an automatic 'dither' feedback, which makes up/down changes to the multiknobs, and determines their effect on the luminosity from the correlated variation of the beamstrahlung-induced energy loss [105].

13.2 Beta Optimization

Suppose, at N positions around the ring, the deviation of the beta function from its design value, $\Delta\beta$, has been measured. One way of correcting the errors found is to explicitly identify the source of the optics error using the techniques discussed in Section 5.4.

A different approach is to use the calculated (or measured) sensitivity matrix S of N different β values to a set of M independently powered quadrupoles or quadrupole families, with gradients $k_1, \ldots, k_M$. To correct the optics, the gradient changes required, $\mathbf{\Delta k} = (\Delta k_1, \ldots, \Delta k_M)$, should fulfill the equation

$$-\begin{pmatrix} \Delta\beta_1 \\ \Delta\beta_2 \\ \ldots \\ \Delta\beta_N \end{pmatrix} = \begin{pmatrix} S_{11} & S_{12} & \ldots & S_{1M} \\ S_{21} & S_{22} & \ldots & S_{2M} \\ .. & & & \\ S_{N1} & S_{N2} & \ldots & S_{NM} \end{pmatrix} \begin{pmatrix} \Delta k_1 \\ \Delta k_2 \\ \ldots \\ \Delta k_M \end{pmatrix} \tag{113}$$

The optimum correction vector $\mathbf{\Delta k} = (\Delta k_1, ..., \Delta k_M)$ is obtained from Eq. (113), for example, by means of a singular value decomposition.

13.3 Multiknobs

A problem frequently encountered in practice is to correct an aberration or to match one optical function without degrading other ones. For example, we may want to cancel a residual dispersion without affecting the beta functions. This can be done very efficiently by using a multiknob. A multiknob is a combination of quadrupoles and skew quadrupoles (or possibly dipole correctors, sextupoles, even octupoles,...), which are changed together, with the proper ratio and relative sign, in such a way that only the aberration of interest is generated.

Such knobs are very powerful. For example, by scanning a dispersion knob, one can minimize the beam size on some profile monitor or wire scanner downstream, thus eliminating any residual dispersion. In a ring, similar knobs may be used to correct skew coupling and dispersion: by minimizing the beam size on a synchrotron light monitor with these knobs, the vertical equilibrium emittance can be reduced.

The knob coefficients may be calculated in a variety of ways. A simple approach is to use the matching functions of the MAD program[44], to determine the relative changes in quadrupole strengths required to vary the parameter of interest (such as the beta function or the dispersion at some position).

A second approach to generate multiknobs is to use SVD. The problem

can be cast into a matrix equation of the form

$$\left(\begin{array}{c} \Delta\beta_x \\ \Delta\alpha_x \\ \Delta\mu_x \\ \Delta\eta_x \\ \Delta\eta'_x \\ \Delta\beta_y \\ \Delta\alpha_y \\ \Delta\mu_y \\ \Delta\eta_y \\ \Delta\eta'_y \\ \cdots \end{array} \right)_{s=s_0} = \left(\begin{array}{cccc} B_{11} & B_{12} & \cdots & B_{1N} \\ B_{21} & B_{22} & \cdots & B_{2N} \\ & \cdots & \cdots & \\ B_{M1} & B_{M2} & \cdots & B_{MN} \end{array} \right) \left(\begin{array}{c} \Delta k_1 \\ \Delta k_2 \\ \cdots \\ \Delta k_N \end{array} \right) \tag{114}$$

The sensitivity matrix **B** could either be obtained from an optics model, or it could be determined empirically on the machine. For a good match, the number of adjustbale parameters should be larger or equal to the number of constraints. So, unless there is some optical symmetry, one must have $N \geq M$.

Equation (114) is of the same form as Eq. (108). Thus, if, for example, we want to create a dispersion knob which changes $\Delta\eta_x$ by 1 mm at location $s = s_0$, and which keeps all other parameters constant, we can solve this problem by a singular value decomposition. The latter will determine a set of changes in the quadrupole strengths $(\Delta k_1, \ldots, \Delta k_N)$, which fulfills the objective and which simultaneously minimizes the overall magnitude of the changes, *i.e.*, the sum $\sum_i (\Delta k_i)^2$. This scheme can be generalized to include higher order optics in an obvious way.

The knob coefficients are calculated only for small changes to the intermediate optics. If many quadrupoles are part of the knob, the R matrices between them will change as the knob is being varied. This means the coefficients determining the knob are not constant, but change depending on the knob setting. If needed, this problem can be overcome by using nonlinear knobs, where the differential change in quadrupole strengths is recalculated in many small steps, effectively performing an integration of Eq. (114), in order to determine the final quadrupole values at the desired knob setting. Such nonlinear knobs were developed for the SLC final focus [107].

13.4 Diagnostic Pulse

At the SLC, a diagnostic pulse is used to monitor, quasi-continuously, the stability of the linac optics [108]. Every few minutes fast kickers induce betatron oscillations for individual selected bunches, prior to their injection into the

linac. The propagation of the measured betatron oscillations along the linac is recorded, and then decomposed into an amplitude and a phase component. The inferred betatron phase advance along the linac is a very sensitive indicator of optics changes, which may be caused by, *e.g.*, variations in the linac energy profile, or in beam current, bunch length, and bunch distribution.

14 Model-Independent Diagnostics

Some accelerators may be so complex and their optics so variable that it is not possible to establish a model which reproduces the reality sufficiently well over longer periods of time to be useful for diagnostics and monitoring purposes. A good example of such a situation is the SLAC linac. Here, details of the beam energy profile along the linac are not precisely known, because individual klystron phases may drift in time (a klystron is an rf power source; the SLC has more than 200). Therefore, the normalized quadrupole gradients are not fully determined. Also transverse and longitudinal wakefields change the optics depending on bunch charge, bunch distribution and orbit.

A way out in such a condition is to employ a model-independent analysis of the orbit data. Here, no attempt is made to accurately determine the parameter set for an optics model, but the beam information and the beam response to certain perturbations are used directly to monitor the accelerator stability, to determine misalignments of accelerator structures and so on.

A very interesting approach is currently being developed at SLAC by J. Irwin, C.-X. Wang, Y. Yan *et al.* [109,110]. The primary quantity on which the analysis is based is a matrix of BPM readings $\mathbf{B}$, where

$$\mathbf{B} = \begin{pmatrix} b_{11} & b_{12} & \dots & b_{1m} \\ & \dots & \dots & \\ b_{p1} & b_{p2} & \dots & b_{pm} \end{pmatrix} \tag{115}$$

has m columns, representing m different BPMs, and p rows, for p different beam pulses. In an actual application m may be of the order of 100 and p can be several 1000. There are many contributions to $\mathbf{B}$, for example changes in the initial conditions, changes in the beamline components, ground motion, BPM noise etc.

One can assume a linear (or quadratic) expansion of the form

$$\mathbf{b_i} = \mathbf{b_0} + \sum_{s=1}^{S} \Delta\hat{q}_i^s \left[\sigma_s \frac{\partial \mathbf{b}}{\partial q^s}\right] + \text{noise} \tag{116}$$

where $\mathbf{b}$ denotes a row vector of the matrix $\mathbf{B}$, $\hat{q}^s$ represents the sth variable affecting the BPM readings (such as an incoming betatron oscillation, or

klystron amplitude), and σ_s the rms variation of this perturbation. The variable $\hat{q}_i^s$ is normalized so that the rms value over time is one, or $< \hat{q}^s >_{\rm rms} = 1$, and $< \Delta q_s >_{\rm rms} = \sigma_s < \hat{q}^s >_{\rm rms} = \sigma_s$.

The above equation can be rewritten in matrix form as

$$\mathbf{B} = \mathbf{Q} \cdot \mathbf{F}^t + \eta \tag{117}$$

where now η represents the BPM noise, and the rows of the matrix $\mathbf{F}^t$ are the sensitivity vectors $\mathbf{f} = [\sigma_s \partial \mathbf{b} / \partial q^s]$, weighted according to the amount of variation (σ_s) detected in each variable.

The relative contribution of different variables q^s to the observed orbit variation can be identified fairly easily, provided certain tagging signals $\mathbf{t_i}$ (*e.g.*, the bunch length, energy, or the incoming betatron oscillation inferred from the first few BPMs) are available and correlated to one (or more) of the source perturbations $\mathbf{f}_j$. For example, suppose the beam phase ϕ and the current I are the tagging signals, and further suppose that their mutual correlation is not zero $< \Phi I > \neq 0$, but that they are uncorrelated with all other perturbations. In that case one can multiply the matrix $\mathbf{B}$ by the two normalized tagging vectors $(\hat{\phi}, \hat{\mathbf{I}})$, obtaining

$$\begin{pmatrix} \hat{\mathbf{I}} \\ \hat{\phi} \end{pmatrix} \mathbf{B} = \begin{pmatrix} 1 & < \hat{\mathbf{I}} \hat{\phi} > & \dots \\ < \hat{\mathbf{I}} \hat{\phi} > & 1 & \dots \end{pmatrix} \begin{pmatrix} \mathbf{f}_I \\ \mathbf{f}_\phi \end{pmatrix} + \mathcal{O}\left(\frac{\sigma}{\sqrt{p}} \right) \tag{118}$$

Equation (118) can be inverted, up to terms of order $\sigma/\sqrt{p}$. This inversion is of great interest because it provides the explicit 'space pattern' (shape) and the magnitude of the two orbit perturbations corresponding to changes in current or phase: $\mathbf{f_I}$, and $\mathbf{f}_\phi$.

For more refined studies, the SVD technique is again of great use. For example, via SVD, we can decompose the matrix $\mathbf{B}$ as

$$\mathbf{B} = \mathbf{U}(\mathbf{W}\mathbf{V}^t) \tag{119}$$

where $\mathbf{U}$ now represents the 'time patterns' (equivalent to $\mathbf{Q}$) and $(\mathbf{W}\mathbf{V}^t)$ the 'space patterns' (equivalent to $\mathbf{F}^t$) [109]. If we calculate the significant SVD eigenvalues w_j of the matrix $\mathbf{W}$ for an increasing number of BPMs (in the order of their position along the beamline), we can find locations where additional eigenvalues become large. These are the locations where additional orbit jitter is introduced, for example by an oscillating corrector or by a structure misalignment converting bunch length variation into orbit variation etc.

It is expected that in the future this method will allow us to determine the alignment of all structures along the SLAC linac. Similar methods could of course be applied to storage rings.

15 Acknowledgements

I would like to thank R. Assmann, R. Bartolini, C. Bovet, H. Burkhardt, Y. Cai, J. Corbett, M. Donald, P. Emma, M. Giovannozzi, K. Hirata, A. Hofmann, B. Holzer, J. Irwin, H. Koiso, O. Meincke, M. Minty, K. Oide, T. Raubenheimer, I. Reichel, J. Safranek, M. Seidel, P. Tenenbaum, D. Whittum, U. Wienands, and Y. Yan for valuable informations, stimulating discussions, for providing most of the material presented and for permitting its use in this lecture. I am grateful to numerous further colleagues at SLAC, in particular those working on SLC, PEP-II and SPEAR for their untiring support, cooperation and inspiration. Finally, I am very grateful to M. Minty, N. Phinney and D. Whittum for reading a draft of the manuscript, making many helpful suggestions, correcting several mistakes, and smoothening the English.

16 References

1. S. Myers, "The LEP Collider, from Design to Approval and Commissioning", CERN Accelerator School, 6th John Adams Memorial Lecture, CERN-91-08 (1991).
2. "PEP-II An Asymmetric B Factory", SLAC-418 (1993).
3. "KEKB B-Factory Design Report", KEK Report 95-7 (1995).
4. J.T. Seeman, "The Stanford Linear Collider", Ann. Rev. Nucl. Part. Sci. 40, p. 389 (1990).
5. P. Emma, "The Stanford Linear Collider", Proc. of 1995 IEEE PAC, Dallas, p. 606 (1995).
6. Y. Kimura, "Status of Tristan", Proc. of the XVth International Conference on High Energy Accelerators, Hamburg, p. 72 (1992).
7. SPEAR Storage Ring Group, "SPEAR: Status and Improvement Program", Proc. of IXth Conference International Conference on High Energy Accelerators, Stanford, p. 37 (1974).
8. F. Hinode *et al.*, "Accelerator Test Facility–Design and Study Report", KEK Internal Report 95-4 (1995).
9. P. Schmüser, "The Electron-Proton Colliding Beam Facility HERA", Nucl. Instr. Methods A 235, p. 201 (1985).
10. M. Berndt, *et al.*, "Final Focus Test Beam: Project Design Report", SLAC-0376 (1991).
11. J. Gareyte, "The SPS P Anti-P Collider", Proc. of Antiprotons for Colliding Beam Facilities, CERN, Geneva, 1983, CERN report 84-15 (1984).
12. C. Adolphsen, *et al.*, "Measurement of Wake Field Suppression in an Detuned X Band Accelerator Structure", Phys. Rev. Letters 74, p. 2475

(1995).
13. K. Johnsen, "Present Status and Future Plans for the ISR", Proc. of IXth Conference International Conference on High Energy Accelerators, Stanford, p. 32 (1974).
14. E.D. Courant and H.S. Snyder, "Theory of the Alternating-Gradient Synchrotron", Annals of Physics 3, 1-48 (1958).
15. M. Sands, "The Physics of Electron Storage Rings", SLAC-121 (1970)
16. K.L. Brown, "A First and Second-Order Matrix Theory for the Design of Beam Transport Systems and Charged Particle Spectrometers", SLAC-75 (1982).
17. K.L. Brown, F. Rothacker, D. Carey, C. Iselin, "Transport. A Computer Program for Designing Charged Particle Beam Transport Systems", SLAC-91 (1977).
18. F. Zimmermann, P. Krejcik, M. Minty, D. Pritzkau, T. Raubenheimer, M. Ross, M. Woodley, "Ion Effects in the SLC Electron Damping Ring under Exceptionally Poor Vacuum Conditions", Proc. of the International Workshop on Multibunch Instabilities in Future Electron and Positron Accelerators (MBI97), Tsukuba, and SLAC-PUB-7665 (1997).
19. T. Ieiri and K. Hirata, "Observation and Simulation of Nonlinear Behavior of Betatron Oscillations During the Beam-Beam Collision", Proc. of the 1989 IEEE PAC (1989).
20. E. Asseo, CERN PS/85-3 (LEA) (1985).
21. R. Bartolini, M. Giovannozzi, W. Scandale, A. Bazzani, E. Todesco, "Algorithms for a Precise Determination of the Betatron Tune", Proc. of EPAC 96, Sitges, vol. II, p. 1329 (1996). see also CERN report SL/95-84 (1995).
22. F. J. Harris, "On the Use of Windows for Harmonic Analysis with Discrete Fourier Transform", Proc. IEEE Vol. 66, No 1, January 1978.
23. J. Byrd, "Longitudinal Beam Transfer Function Diagnostics in an Electron Storage Ring", Particle Accelerators (1998).
24. G. Carron, D. Möhl, Y. Orlov, F. Pedersen, A. Poncet, S. van der Meer, D.J. Williams, "Observation of Transverse Quadrupole Mode Instabilities in Intense Cooled Antiproton Beams in the AA", CERN/PS/89-18 (1989).
25. H. Schmickler, "Diagnostics and Control of the Time Evolution of Beam Parameters", presented at the Third European Workshop on Beam Diagnostics and Instrumentation at Particle Accelerators (DIPAC 97) and CERN-SL-97-68 (1997).
26. C. Boccard et al., "Tune Measurements in the SPS as Multicycling machine", Proc. of EPAC96, Sitges (1996).

27. K.D. Lohmann et al., "Design and functionality of the LEP Q-meter", Proc. of EPAC90, Nice (1990).
28. J. Borer and R. Jung, "Diagnostics", CERN Accelerator School on Antiprotons for Colliding Beam Facilities, CERN 84-15, p. 385 (1984)
29. R. Bartolini, M. Giovannozzi, W. Scandale, A. Verdier, C. Pellegrini, P. Tran, E. Todesco, J. Corbett, M. Cornacchia, "Measurements of the Tune Variations Induced by Non-Linearities in Lepton Machines", Proc. of EPAC 96, Sitges, vol. II, p. 917 (1996).
30. J. Bengtsson, "Spectral Analysis of the Motion at a Single Nonlinear Resonance by Canonical Perturbation Theory", CERN internal report PS/LEA/Note 87-03 (1987).
31. C.-X. Wang and J. Irwin, "Possibility to measure the Poincaré section map of a circular accelerator", submitted to Physical Review E, and SLAC-PUB-7547 (1997).
32. R. Bartolini and F. Schmidt, "Normal Form via Tracking or Beam Data", Part. Accelerators (in press) and LHC Project Report 132 (1997).
33. Y. Cai, "Lattice Performance of the PEP-II High Energy Ring", presented at the Advanced ICFA Beam Dynamics Workshop on Beam Dynamics Issues for e^+e^- Factories, Frascati, Italy, and SLAC-PUB-7733 (1997).
34. J. Borer, C. Bovet, A. Burns, G. Morpurgo, "Harmonic Analysis of Coherent Bunch Oscillations at LEP", Proc. of EPAC92, p. 1082 (1992).
35. D. Brandt, P. Castro, K. Cornelis, A. Hofmann, G. Morpugo, G.L. Sabbi, J. Wenninger, and B. Zotter, "Measurements of Impedance Distributions and Instability Thresholds in LEP", Proc. of 1995 IEEE PAC, Dallas, p. 570 (1995).
36. K. Oide, private communication (1997).
37. P. Castro, "Betatron Function Measurement at LEP Using the BOM 1000 Turns Facility", SL/Note 92-63 (1992).
38. J. Corbett, private communication (1998).
39. Y. Cai, private communication (1998).
40. Y. Cai, M. Donald, J. Irwin, Y. Yan, "LEGO: A Modular Accelerator Design Code", Proc. of IEEE PAC97, Vancouver, and SLAC-PUB-7642 (1997).
41. The RESOLVE program was written by M. Lee.
42. J. Safranek, "Experimental determination of storage ring optics using orbit response measurements", Nucl. Instr. and Meth. A388, 27 (1997).
43. J. Safranek, these proceedings.
44. H. Grote, F.C. Iselin, The MAD Program, Version 8.1, CERN/SL/90-13, 1991.

45. M. Donald, private communication (1998).
46. S. Kamada, "Overview on Experimental Techniques and Observations", Proc. of workshop on Nonlinear Dynamics in Particle Accelerators: Theory and Experiments", Arcidosso, Italy (1994).
47. H. Koiso, H. Fukuma, Y. Funakoshi, S. Kamada, S. Matsumoto, K. Oide, and N. Yamamoto, "Beam-Based Measurement of Strength Errors in Quadrupole Magnets with Orbit Bumps", Proc. of EPAC 96, Sitges, Spain (1996).
48. E.-S. Kim and S. Matsumoto, "Beam-Based Measurement of Focusing Errors in Quadrupole Magnets in ATF Damping Ring", in the Proc. of the 2nd ATF International Collaboration Meeting", KEK, Tsukuba, KEK Proceedings 97-9, p. 82 (1997).
49. C. Bovet, "The Measurement of some Machine Parameters", in J. Bosser (ed.), "Beam Instrumentation", CERN-PE-ED 001-92 (1992), rev. (1994).
50. T. Lohse and P. Emma, "Linear Fitting of BPM Orbits and Lattice Parameters", SLAC Single Pass Collider Memo CN-371 (1989).
51. T. Barklow, P. Emma, P. Krejcik, N. Walker, "Review of Lattice Measurement Techniques at the SLC", presented at the 5th ICFA Advanced Beam Dynamics Workshop, Corpus Christi, Texas (1991).
52. M. Sands, "A Beta Mismatch Parameter", SLAC internal report SLAC-AP-85 (1991).
53. W. Spence, private communication (1996).
54. R. Iverson, M. Minty, M. Woodley, private communication, and ATF internal report ATF 12-29 (1997).
55. M. Minty *et al.*, "Damping Time Measurements using a Fast Gated Camera", AIP Conf. Proc., 281 J.A. Hinkson and G. Stover eds., Accelerator Instrumentation Workshop, Berkeley, p. 158 (1992).
56. M.G. Minty and W.L. Spence, "Injection Envelope Matching in Storage Rings", Proc. of 1995 IEEE PAC, Dallas, p. 536 (1995).
57. R. Brinkmann and M. Böge, "Beam-Based Alignment and Polarization Optimization in the HERA Electron Ring", Proc. of EPAC94, London, p. 938 (1994).
58. D.P. Barber, R. Brinkmann, E. Gianfelice, T. Limberg, N. Meyners, P. Schuüler, M. Spengos, M. Böge, "Application of a Beam-Based Alignment Technique for Optimizing the Electron Spin Polarization at HERA", Proc. of EPAC96, Sitges, p. 439 (1996).
59. D. Robin, G. Portmann, L. Schachinger, "Automated Beam Based Alignment of the ALS Quadrupoles", internal SLAC Report, NLC-Note 18 (1995).

60. J. Corbett, R.O. Hettel, H.-D. Nuhn, "Quadrupole Shunt Experiments at SPEAR", Proc. of 7th Beam Instrumentation Workshop (BIW96), Argonne, Illinois (1996).
61. P. Emma, "Beam-Based Alignment of Sector-1 of the SLAC Linac", Proc. of EPAC 92, Berlin, and SLAC-PUB-5787 (1992).
62. I. Reichel, "Beam Position Measurement by Modulation of Quadrupole Strengths", SL note/95-50 (1995).
63. P. Emma, J. Irwin, N. Phinney, P. Raimondi, N. Toge, N.J. Walker, V. Ziemann "Beam Based Alignment of the SLC Final Focus Sextupoles", Proc. of 1993 IEEE PAC, Washington, DC, p. 116 (1993).
64. M. Kikuchi, K. Egawa, H. Fukuma, M. Tejima, "Beam-Based Alignment of Sextupoles with the Modulation Method", Proc. of 1995 IEEE PAC, Dallas, p. 603 (1995).
65. N. Yamamoto, S. Kamada, Y. Kobayashi, H. Koiso, and S. Matsumoto, "Beam-Based Alignment of Sextupole Magnets with a π-Bump Orbit", KEK Preprint 96-74 (1996).
66. S. Herb, G.B. Jaczko, and F. Willeke, "Beam-Based Calibration of Beam Position Monitor Offsets in the HERA Proton Ring using Strong Sextupole Fields", Proc. of workshop on Beam Diagnostics and Instrumentation for Particle Accelerators, Travemuende, DESY Int. Rep. M-95-07 (1995).
67. T. Raubenheimer, in the Zeroth Order Design Report for the Next Linear Collider, SLAC Report 474, p. 227-228 (1995).
68. P. Emma, J. Irwin, N. Phinney, P. Raimondi, N. Toge, N.J. Walker, V. Ziemann, "Beam Based Alignment of the SLC Final Focus Sextupoles", Proc. of IEEE PAC 93, Washington, D.C. (1993).
69. P.G. Tenenbaum, "Expanded Studies of Linear Collider Final Focus Systems at the Final Focus Test Beam", SLAC-R-95-475 (1995).
70. M. Seidel, C. Adolphsen, K.L.F. Bane, R.M. Jones, N.M. Kroll, R.H. Miller, D.H. Whittum, "Absolute Beam Position Measurement in an Accelerator Structure", Nucl. Instr. Methods A 404, p. 231 (1998).
71. F. Ruggiero, "Effect of Residual Dispersion at the RF Cavities on the Dynamic Measurement of Dispersion in LEP", CERN SL/91-38 (1991).
72. M. Minty, unpublished (1997).
73. K. Kubo and T. Okugi, "Dispersion Measurement in ATF DR", ATF Internal Report ATF-97-19 (1997).
74. P. Emma and W. Spence, Proc. of the SLAC/KEK Linear Collider Workshop on Damping Ring, Tsukuba, KEK Proceedings 92-6 (1992).
75. E. Perevedentsev, these proceedings.
76. U. Wienands, private communication (1998).

77. A. Fisher, A. Lumpkin, B. Zotter, J. Byrd, J. Hinkson, R. Assmann, unpublished (1998).
78. R. Assmann, *et al.*, "The Energy Calibration of LEP in the 1993 Scan", submitted to Zeitschrift für Physik, CERN-SL/95-02 (1995).
79. A. Hofmann, private communication (1998).
80. O. Meincke, S. Herb, and P. Schmüser, "Chromaticity Measurements in the HERA Proton Storage Ring", Proc. of EPAC 92, Berlin, p. 1070 (1992).
81. A. Piwinski, S. Herb, *et al.*, measurements at DORIS-I and HERA.
82. For LEP this measurement was proposed by A. Hofmann.
83. C. Zhang, W.F. Du, Z.G. Cai, "Beam Energy Stabilization and Online Measurement in BEPC", Proc. of the XVth International Conference on High Energy Accelerators, Hamburg, p. 409 (1992).
84. H. Schmickler, "Measurement of the Central Frequency of LEP", CERN LEP performance note 89 (1993).
85. G. Ripken, F. Willeke, "On the Impact of Linear Coupling on Nonlinear Dynamics", DESY 90-001 (1990).
86. F. Willeke and G. Ripken, "Methods of Beam Optics", Cornell Summer School, AIP Proceedings 184, and DESY 88-114 (1988).
87. G. Ripken, "Untersuchungen zur Strahlführung und Stabilität der Teilchenbewegung in Beschleunigern und Storage-Ringen unter strenger Berücksichtigung einer Kopplung der Betatronschwingungen", Int. Rep. DESY R1-70/4 (1970).
88. D.A. Edwards and L.C. Teng, "Parametrization of Linear Coupled Motion in Periodic Systems", IEEE Trans. on Nucl. Sc. 20, p. 885 (1973).
89. L.C. Teng, "Concerning n-dimensional coupled Motion", Fermilab internal report FN 229 (1971).
90. G. Guignard, "The General Theory of All Sum and Difference Resonances in a Three-Dimensional Magnetic Field in a Synchrotron", CERN 76-06 (1976).
91. T. Raubenheimer, "Tolerances to Limit the Vertical Emittance in Future Storage Rings", Part. Acc. 36, p. 75 (1991).
92. P. Bryant, "A Simple Theory for Weak Betatron Coupling", CERN Accelerator School, CERN 89-05 (1989)
93. M.G. Minty, H. Hayano and F. Zimmermann, "Measurements of Betatron Coupling at the ATF Damping Ring", ATF internal report, in preparation (1998).
94. G. Bourianoff, S. Hunt, D. Mathieson, F. Pilat, R. Talman, G. Morpugo, "Determination of Coupled-Lattice Properties Using Turn-by-Turn Data", Proc. of the workshop on the stability of particle motion in storage

rings, Upton, NY 1992, AIP Conference Proceedings 292 (1992).
95. J. Seeman *et al.*, unpublished (1997).
96. J.P. Koutchouk, "Linear Betatron Coupling Measurement and Compensation in the ISR", CERN ISR-OP/80-27, also published in the Proc. XIth Int. Conf. on High Energy Accelerators, CERN, Geneva, Birkhäuser Verlag, Basel, p. 491 (1980).
97. J. Turner, private communication (1998).
98. V. Ziemann, "Corrector Ironing", SLAC internal report Single-Pass Collider Note CN-393 (1992).
99. W. Press, *et al.*, "Numerical Recipes", Section 2.9, Cambridge University Press, Cambridge (1986).
100. The MathWorks, Inc. (1994).
101. W.J. Corbett, F. Fong, M. Lee, V. Ziemann, "Optimum Steering of Photon Beam Lines in SPEAR", Proc. of 1993 IEEE PAC Washington, p. 1483 (1983).
102. M. Minty, C. Adolphsen, L.J. Hendrickson, R. Sass, T. Slaton, M. Woodley, "Feedback Performance at the Stanford Linear Collider", Proc. of IEEE PAC 95, Dallas (1995).
103. T. Himel, "FEEDBACK: Theory and Accelerator Applications", Annu. Rev. Nucl. Part. Sci. 47, p. 157 (1997).
104. P. Emma, L.J. Hendrickson, P. Raimondi, F. Zimmermann, "Limitations of Interaction-Point Spot-Size Tuning at the SLC", to be published in the Proceedings of the 17th IEEE Particle Accelerator Conference (PAC 97), Vancouver, Canada, 12 - 17 May, 1997, SLAC-PUB-7509 (1997).
105. L. Hendrickson *et al.*, "Luminosity Optimization Feedback in the SLC", Proc. of ICALEPCS 1997 (1997).
106. W.A. Koska, P. Bambade, W. Kozanecki, N. Phinney, S.R. Wagner, "Beam-Beam Deflection as a Beam Tuning Tool at the SLAC Linear Collider", Proc. of 1989 IEEE PAC, Chicago, Nucl. Instrum. Meth. A 286, p. 32 (1990).
107. N.J. Walker, J. Irwin, M. Woodley, "Global Tuning Knobs for the SLC Final Focus", Proc. of 1993 IEEE PAC, Washington (1993).
108. R.W. Assmann, F.-J. Decker, L.J. Hendrickson, N. Phinney, R.H. Siemann, K.K. Underwood, M. Woodley, "Beam-Based Monitoring of the SLC Linac Optics with a Diagnostic Pulse", Proc. of IEEE PAC 97, Vancouver, and SLAC-PUB-7578 (1997).
109. C.X. Wang, J. Irwin, Y. Yan *et al.*, report in preparation for EPAC 98.
110. C.X. Wang, Ph.D. thesis, SLAC, in preparation.